PREDICTION OF LOW-CYCLE FATIGUE LIFE BASED ON UNCOUPLED DUCTILE FRACTURE CRITERIA

A THESIS SUBMITTED TO
THE GRADUATE SCHOOL OF NATURAL AND APPLIED SCIENCES
OF
MIDDLE EAST TECHNICAL UNIVERSITY

BY

OZAN GÜNDÜZ

IN PARTIAL FULFILLMENT OF THE REQUIREMENTS
FOR
THE DEGREE OF MASTER OF SCIENCE
IN
MECHANICAL ENGINEERING

SEPTEMBER 2024

Approval of the thesis:

PREDICTION OF LOW-CYCLE FATIGUE LIFE BASED ON UNCOUPLED DUCTILE FRACTURE CRITERIA

submitted by **OZAN GÜNDÜZ** in partial fulfillment of the requirements for the degree of **Master of Science** i**n Mechanical Engineering, Middle East Technical University** by,

Prof. Dr. Naci Emre Altun
Dean, **Graduate School of Natural and Applied Sciences** _____

Prof. Dr. Serkan Dağ
Head of the Department, **Mechanical Engineering** _____

Prof. Dr. Haluk Darendeliler
Supervisor, **Mechanical Engineering, METU** _____

Asst. Prof. Dr. Şehram Dizeci
Co-Supervisor, **Mechanical Engineering, TEDU** _____

Examining Committee Members:

Prof. Dr. Fevzi Suat Kadıoğlu
Mechanical Engineering, METU _____

Prof. Dr. Haluk Darendeliler
Mechanical Engineering, METU _____

Prof. Dr. Can Çoğun
Mechanical Engineering, Çankaya University _____

Assoc. Prof. Dr. Ulaş Yaman
Mechanical Engineering, METU _____

Asst. Prof. Dr. Orkun Özşahin
Mechanical Engineering, METU _____

Date: 03.09.2024

I hereby declare that all information in this document has been obtained and presented in accordance with academic rules and ethical conduct. I also declare that, as required by these rules and conduct, I have fully cited and referenced all material and results that are not original to this work.

Name Last name : Ozan Gündüz

Signature :

ABSTRACT

PREDICTION OF LOW-CYCLE FATIGUE LIFE BASED ON UNCOUPLED DUCTILE FRACTURE CRITERIA

Gündüz, Ozan
Master of Science, Mechanical Engineering
Supervisor : Prof. Dr. Haluk Darendeliler
Co-Supervisor: Asst. Prof. Dr. Şehram Dizeci

September 2024, 78 pages

Classical life prediction methods to determine fatigue failure require extensive testing, which increases costs and time. This thesis aims to estimate low-cycle fatigue failure by developing a fatigue failure criterion (FFC) based on uncoupled ductile fracture criteria (UDFC) and numerical simulations of tensile test specimens made of the relevant materials. For this purpose, five energy-based UDFC namely Freudenthal, Cockroft-Latham, Ayada, Oyane-Sato, and Oh are used. A user-defined subroutine is written and implemented to FEA software for calculating the damage accumulation related to these criteria for both quasi-static and cyclic loading. Then, damage accumulation values of both the tensile test simulations and fatigue simulations for the sample material are obtained and compared using the mentioned five UDFC. Fatigue simulations are carried out for different stress amplitude, mean stress and frequency values. All comparisons are conducted by referring to the values obtained at the onset of necking which is determined by the stress wave propagation method. As a result, an equation is obtained that defines the failures calculated by these five UDFC under various stress amplitude and mean stress values. This equation is called as fatigue failure criterion function and can be presented by a

surface to define the failure. FFC function is also used to determine the fatigue life for the low-cycle by another relation called the life function. Finally, this function is applied to determine the FFC for fatigue failure. It is observed that damage accumulation can be calculated using FFC with acceptable accuracy.

Keywords: Low-Cycle Fatigue, Plasticity, Ductile Damage, Life Prediction, Stress Wave Propagation Method

ÖZ

DÜŞÜK ÇEVRİMLİ YORULMA ÖMRÜNÜN AYRIK SÜNEK KIRILMA KRİTERLERİNE DAYALI TAHMİNİ

Gündüz, Ozan
Yüksek Lisans, Makina Mühendisliği
Tez Yöneticisi: Prof. Dr. Haluk Darendeliler
Ortak Tez Yöneticisi: Dr. Öğr. Üyesi Şehram Dizeci

Eylül 2024, 78 sayfa

Yorulma hasarını belirlemek için kullanılan klasik ömür tahmin yöntemleri, maliyetleri ve zamanı artıran kapsamlı testler gerektirir. Bu tez, ayrık sünek kırılma kriterlerine (UDFC) ve ilgili malzemelerden yapılmış çekme testi numunelerinin sayısal simülasyonlarına dayalı bir yorulma kırılma kriteri (FFC) geliştirerek düşük çevrimli yorulma hasarını tahmin etmeyi hedeflemiştir. Bu amaçla Freudenthal, Cockroft-Latham, Ayada, Oyane-Sato ve Oh olmak üzere beş enerji bazlı UDFC kullanılmıştır. Hem yarı-statik hem de döngüsel yükleme için bu kriterlere ilişkin hasar birikimini hesaplamak amacıyla kullanıcı tanımlı bir alt program hazırlanarak SEA yazılımına uygulanmıştır. Örnek malzeme için çekme testi simülasyonlarının ve yorulma simülasyonlarının her ikisi için hasar birikim değerleri elde edilmiş ve bahsedilen beş UDFC kullanılarak karşılaştırılmıştır. Yorulma simülasyonları, farklı gerilme genliği, ortalama gerilme ve frekans değerleri kullanılarak gerçekleştirilmiştir. Tüm karşılaştırmalar, gerilme dalgası yayılım yöntemiyle belirlenen boyun verme başlangıcında elde edilen değerlere bakılarak yapılmıştır. Sonuç olarak, bahsedilen beş UDFC kullanılarak çeşitli gerilme genlikleri ve ortalama gerilme değerleri altında hesaplanan hasarları tanımlayan bir denklem elde

edilmiştir. Bu denklem yorulma hasar kriteri fonksiyonu olarak adlandırılmıştır ve hasarı tanımlamak için bir yüzey ile ifade edilebilmektedir. FFC fonksiyonu, düşük çevrim için yorulma ömrünü, ömür fonksiyonu olarak adlandırılan başka bir denklem ile belirlemek için de kullanılmıştır. Son olarak bu fonksiyon yorulma hasarı için FFC belirlemek için uygulanmıştır. FFC kullanılarak hasar birikiminin kabul edilebilir doğrulukla hesaplanabildiği görülmüştür.

Anahtar Kelimeler: Düşük Çevrimli Yorulma, Plastisite, Süneklik Hasarı, Ömür Tahmini, Stres Dalgası Yayılım Metodu

To my family who always supported me

ACKNOWLEDGMENTS

Firstly, I would like to express my deepest gratitude to my supervisor Prof. Dr. Haluk Darendeliler, and my co-supervisor Asst. Prof. Dr. Şehram Dizeci for their support, teachings, and guidance. Their contributions were not limited to this thesis alone; moreover, they enabled me to gain a perspective on engineering and science throughout my master's program.

Further, I would like to thank Servet Şehirli for his contribution and valuable advice on performing structural tests.

I am beyond grateful for the presence of my parents because they always stand by me and together, they become the pole stars of my life by sheding light on my way.

Finally, I thank the love of my life, Sera Tual for the happiness she brings into my life and her endless support.

TABLE OF CONTENTS

LIST OF TABLES

TABLES

LIST OF FIGURES

FIGURES

LIST OF ABBREVIATIONS

ABBREVIATIONS

DFC: Ductile Fracture Criteria

UDFC: Uncoupled Ductile Fracture Criteria

CDFC: Coupled Ductile Fracture Criteria

FFC: Fatigue Failure Criteria

LCF: Low Cycle Fatigue

HCF: High Cycle Fatigue

UTS: Ultimate Tensile Strength

FEM: Finite Element Method

FEA: Finite Element Analysis

LIST OF SYMBOLS

SYMBOLS

Symbol	Explanation	Symbol	Explanation
σ	Stress	E	Elastic Modulus
σ'	Deviatoric Stress	ϑ	Poisson's Ratio
$\bar{\sigma}$	Equivalent Stress	ρ	Density
σ_Y	Yield Stress	C_{FR}	Freudenthal Constant
σ_m	Mean (Hydrostatic) Stress	C_{CL}	Cockroft & Latham Constant
σ^{tr}	Trial Stress	C_A	Ayada Constant
ε	Total Strain	C_{OS}	Oyane &Sato Constant
ε_e	Elastic Strain	C_O	Oh Constant
ε_p	Plastic Strain	l_e	Characteristic Element Length
$\bar{\varepsilon}_p$	Equivalent Plastic Strain	t_{cr}	Critical Time Step
$\bar{\varepsilon}_f$	Equivalent Fracture Strain	u	Displacement
δ	Kronecker Delta	v	Deformation Speed
f	Yield Function	c_w	Speed of Wave
α	Back Stress	c_e	Elastic Wave Speed
$d\lambda$	Plastic Multiplier	c_p	Plastic Wave Speed
J_2	The Second Deviotoric Stress	σ_{max}	Maximum Stress
C_{ep}	Elastoplastic Stiffness Tensor	σ_{min}	Minimum Stress
Q	Stress Saturation	$\Delta\sigma$	Stress Range
b	Stress Saturation Rate	σ_A	Stress Amplitude
c	Hardening Slope	σ_M	Mean Stress (Cyclic Loading)
γ	Hardening Slope Rate		

CHAPTER 1

INTRODUCTION

1.1 Background and Motivation

Fracture is a phenomenon that people witness from the beginning of their life. From an early age, it was learned that under the necessary amount of load, materials experience fracture. However, after the Industrial Revolution, this simple information was not enough since complicated structures and machines such as cars, ships, and aircraft entered into our lives. This has brought the importance of learning fracture for obtaining safe and light structures. Although there were few studies in the early times, the number of studies accelerated the comprehension of fracture. For this purpose, scientists and engineers have been searching how and when fracture begins and propagates under different loading conditions for various materials by using multiple methods. As these methods predict the real-life results successfully, it became possible to design the structure efficiently. However, there are still no comprehensive solutions for some specific failure types. One of these failure types is fatigue failure. In this thesis, the main goal is to obtain an appropriate life predicting method for low-cycle fatigue failure.

In this thesis, it is intended to predict the low-cycle fatigue failure of a material by using energy accumulation in its simple tensile test. Materials exhibit different stress-strain responses because of their different atomic structures and different loading types. For example, responses of metallic and composite structures are different due to the amount of plastic deformation that takes place, or for the same material, responses of uniaxial loading and torsional loading are dissimilar from each other due to existing stress and strain conditions.

Simple tension test is the easiest way to examine stress-strain relation for a metalic structure under uniaxial loading as shown in Figure 1.1. It can be observed that metals experience two different regions called elastic and plastic regions until they undergo fracture. In the elastic region, metals generally have a linear stress-strain relation, and do not undergo permanent deformation after unloading. On the other hand, in the plastic region, materials exhibit a nonlinear stress-strain relation, and when unloading or fracture occurs, permanent deformation remains. When a structure is loaded to fracture with increasing tensile stress, its stress-strain curve progresses elastically until the yield point. However, after the yield point, plastic deformation begins, and up to a top point, which is called as ultimate tensile strength (UTS) point, engineering stress increases. This point marks the onset of necking. From this point to fracture, the cross-sectional area decreases rapidly, and engineering stress values decrease also at the necking location.

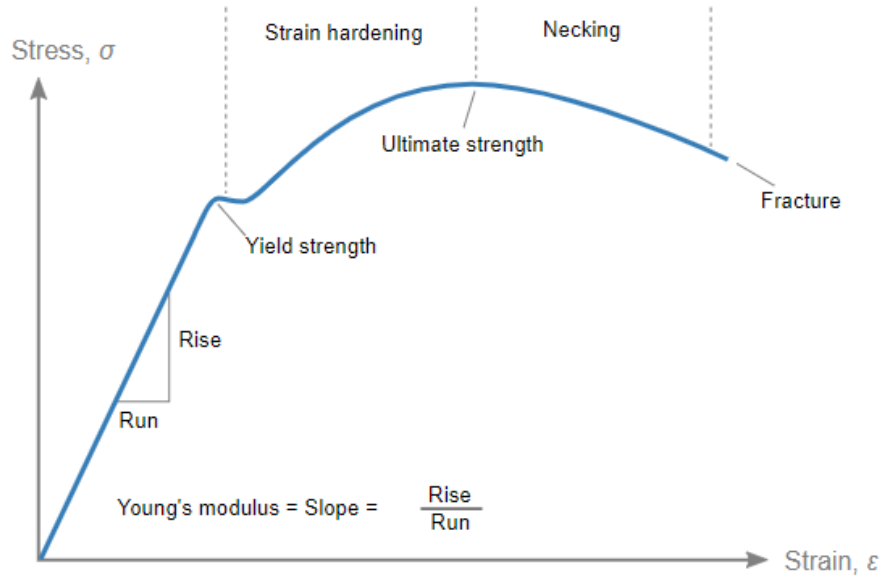

Figure 1.1: Stress-Strain Curve Under Uniaxial Tensile Loading

For most engineering applications, the criteria of structural failure are taken as elastic deformation limit. Otherwise, ductile fracture is the criteria for failure in the plastic region. As long as materials do not reach these limits, they are structurally safe. Most of the structures had been designed by using these rules until fatigue failure was explored.

Fatigue failure is a phenomenon of the failure of structures under cyclic loading. In fatigue failure, yield strength or ductile fracture are not utilized. For a particular amount of stress or strain amplitude, materials can experience failure if enough number of cycles is applied. Designing structures that have infinite life results in high weight, whereas designing structures with respect to only static strength may cause catastrophic failures in the service life of structures due to fatigue. Hence, structures must not endure only maximum loads that they are exposed to, but also cyclic loads of their planned service life.

For static monotonic loading failures, although material limits could be found from tests, stress space that reaches these limits is load and material-dependent. Therefore, there are various damage criteria for predicting failure under different loading conditions and materials. For metallic materials, there are two main ductile damage criteria which are coupled and uncoupled ductile fracture criteria. Coupled ductile fracture criteria are used with the constitutive equations of materials and they are hard to implement in finite element models, whereas uncoupled ductile fracture criteria depend on the formulas that are easy to implement in finite element models [1].

For fatigue failures, there are two main approaches which are stress life and strain life methods. When the number of cycles to failure becomes greater than 1000, it is called high-cycle fatigue (HCF). Whereas if it is smaller than 1000, it is called low-cycle fatigue (LCF) [2]. The stress life method uses the stress range and gives close results compared to experiments for HCF, the same accuracy could not be obtained in the LCF region. Hence, for the LCF region, strain life methods are generally used. These methods use strain range and are effective in determining failure in both the

LCF and HCF regions. Although these methods could be useful for fatigue life prediction, they require lots of experiments in different stress or strain amplitudes.

Since general fatigue methods require lots of tests, in order to decrease the number of experiments for prediction of fatigue life in LCF region, new approaches should be developed. One of these approaches can be use of modified uncoupled ductile fracture criteria.

1.2 The objective of the Thesis

Although there are various methods to determine the fatigue failure, they require lots of long-lasting tests. For finding fatigue life curves, engineers and scientists consume more energy, time, and money than simple structural tests such as uniaxial tensile test. The main objective of this thesis is to minimize the number and duration of tests required to predict low-cycle fatigue life. This is aimed by modifying some of existing uncoupled ductile fracture criteria, conducting a uniaxial tensile test, and use them in FEM simulation.

1.3 Scope of the Thesis

In this thesis, the low-cycle fatigue life of AISI 4140 material is investigated by modifying various uncoupled ductile fracture criteria. These criteria are Freudenthal, Cockroft-Latham, Ayada, Oh, and Oyane-Sato. For this purpose, three uniaxial tensile tests were conducted in the METU Mechanical Engineering Department test laboratory. Moreover, a VUMAT subroutine was written by using the Chaboche and Lamaitre nonlinear kinematic hardening model, necessary constitutive relations, and those mentioned UDFCs. Then, this VUMAT subroutine was implemented into an ABAQUS model to reflect the real-life tests and create data for the method of this thesis.

1.4 Outline of the Thesis

This thesis consists of 7 chapters and references. The content of these chapters are explained as follows:

Chapter 1 gives a brief introduction by explaining the background and motivation, objective, scope, and outline of the thesis.

Chapter 2 is a compilation of previous research related to plasticity, fatigue failure, and ductile damage criteria.

Chapter 3 remarks on the theoretical background of the constitutive relationships, some preliminaries about fatigue, and the ductile failure criteria used in this thesis.

Chapter 4 provides a background for the finite element method and describes the FEM model and user-defined subroutine used for this thesis.

Chapter 5 describes structural tests performed for this thesis and gives the main results of these tests.

Chapter 6 presents the results of numerical analysis and discusses them to obtain a method for life calculation.

Chapter 7 explains the conclusion of the thesis and remarks on future work.

CHAPTER 2

LITERATURE REVIEW

The history of fatigue failure begins with the work of Albert who investigated fatigue failure by conducting cyclic tests on haul trucks in mine shafts in 1837 [3]. Then, similar tests were conducted by Morin on horse-drawn mail coaches in 1853 [4]. Moreover, fatigue was first mentioned as a term by Braithwaite in 1854 [5]. However, the work of Wöhler was a milestone for fatigue failure prediction in 1860. He explained the stress amplitude and mean stress effects on fatigue life and he proposed to use a scatter factor for reducing the probability of failure in the design process for structures under cyclic loading [6]**.** His major impact on fatigue was his test results which include life and stress amplitude values. Although he presented the results in a table, in 1936 Spangenberg plotted them as curves, therefore S-N curves or Wöhler curves were obtained [7]. Even today, S-N curves are widely used for stress-life methods.

S-N curves are obtained for a specific material and its heat treatment condition using various stress amplitude values for life prediction. In S-N curves at some materials, there is a limit for infinite life which is called the endurance limit. There are various studies for determining the infinite life by using stress values. For example, in 1930, Soderberg explained the infinite fatigue life by a linear relationship between stress amplitude and mean stress by using endurance limit, fatigue life and yield strength [8]. Moreover, in 1899, Goodman also explained by a linear relation, he used also stress amplitude and mean stress, however, instead of yield strength, he utilized ultimate tensile strength [9]. In addition to them, in 1911, Gerber explained the relation as a parabola which has two terms. The first term includes the square of

mean stress, UTS and fatigue life, and the other term consists of stress amplitude, endurance limit and fatigue life with a first-order [10].

It has been observed that although stress-life methods have a good accuracy for the prediction of fatigue life in high cycles they are not as successful as in low cycles. As a result, for low cycles, approximately less than 1000 cycles, strain life methods are used. In 1910, Basquin plotted the stress versus endurance graph in a log scale as a straight line and the slope of this graph was called the Basquin's exponent [11]. Then, this stress was converted to elastic strain. Therefore, an elastic strain versus life graph was created. In 1950, Manson and Coffin found that plastic strain amplitude and life can also be expressed as a linear line on a log scale and by considering this, they could combine both elastic and plastic strains in one curve which is the combination of two curves [12]. This curve depends on many constants found from the elastic and plastic parts of the curve, on the other hand, it does not contain the mean stress effects. In 1966 Smith Watson and Topper [13] and in 1978 Morrow added mean stress effects into the strain life equation of Manson and Coffin [14].

Since stress and strain life methods require a significant amount of time and empirical data, many researchers have investigated energy-based approaches to reduce time and cost. In 1920, Jasper stated that the fatigue life depends on the strain energy density in cycles [15]. In 1955, Enomoto proposed that when the total energy in each cycle reaches a specific value of energy failure occurs [16]. In 1966, Stowell related the energy for failure in the tensile test with the fatigue test, and he stated that they were equal [17]. In these proposed approaches, strain energy densities in all cycles were assumed as constant and this made the calculations simple. However, Morrow and Feltner showed that strain energy density was not constant during fatigue life. They found that strain energy density first decreased then became constant and at the end of the life it increased dramatically after a small decrease [18]**.** The main disadvantage for energy calculations was seen as obtaining the hysteresis loop accurately. For this purpose, many researchers aimed to explain the evolution of the stress versus strain curve.

The relationship between stress and strain in the plastic region is more complex than the relation in the elastic region because of the nonlinear behavior and evolution of the yield surface. For this reason, many researchers aimed to explain this relation and its evolution under different loading states. To explain this relation in the plastic region, yield criteria and a hardening rule are needed. In 1851, Henri Tresca stated that yielding begins when the maximum shear stress in the material reaches a critical value [19]**.** Then in 1913, Richard von Mises proposed that yielding starts when the second deviatoric stress invariant reaches a critical value [20]. Although the Tresca yield criterion is more conservative, during experimental tests, it was seen that the von Mises yield criterion gives closer results compared to the Tresca yield criterion [21]. This makes many researchers use and develop the von Mises yield criterion in many applications. For example, in 1952, Ducker and Prager developed von Mises for pressure-dependent materials by proposing their yield criteria [22]. Hardening behavior can be explained by different types of hardening rules which are isotropic hardening, kinematic hardening and combined hardening. Ludwig [23], Prandtl and Reuss [24], Ramberg and Osgood [25], Voce [26], and Johnson and Cook [27] suggested isotropic hardening rules to explain hardening behavior. However, Baushinger stated that isotropic hardening is not capable of simulating material behavior in cyclic loading [28]. Prager's linear kinematic hardening model assumes that the evolution of back stress is linearly related to plastic strain [29]. In 1959, Ziegler made modifications to Prager's model and obtained a nonlinear rule [30]. In addition to them, in 1966, Armstrong and Frederick proposed a model that could cover nonlinear behavior in back stress and the Baushinger effect more accurately [31]. In 1979, Chaboche added multiple backstresses to Armstrong and Fredirick's model [32] and increased the accuracy for complex loadings. The most common combined hardening is the Lemaitre-Chaboche Model proposed in 1985. This model can cover damage evolution, nonlinear behavior and multiaxiality [33]. In addition to this model, the Ohno-Wang Model intorduced in 1993 covered ratcheting behavior more accurately by using additional terms that differ from the Lemaitre-Chaboche model which also accounted for the pressure sensitivity effects [34]**.** However, it did

not consider damage evolution effects explicitly. Lemaitre and Menzel developed a model that considered both damage mechanics and thermodynamic effects [35]**.** As mentioned, there are many yield criteria and hardening rules to simulate plastic region. Among these, the most suitable one that verifies the experimental tests can be preferred to model the stress-strain relation from yielding to fracture. However, a fracture cannot be found by using these models.

To find fracture point in quasi-static monotonic loading, many researchers have suggested different fracture criteria for brittle and ductile materials. The ductile fracture criteria can be categorized by coupled and uncoupled ones. In coupled ductile fracture criteria (CDFC), the criteria are implemented to material constitutive relations. The continuum damage mechanics (CDM) and the Gurson-Tvergaard-Needleman (GTN) are the two most popular CDFCs. The CDM model was first introduced by Kachanov in 1958, and it states that the void density in a structure is the main parameter for determining the fracture [36]. The GTN model that was created by Gurson, Tvergaard and Needleman explains ductile fracture with void volume fraction [37]**.** Since CDFCs are hard to implement into FEM, many researchers suggested uncoupled ductile fracture criteria (UDFC) since this kind of criteria can be explained empirically or semi-empirically. The first UDFC was an energy-based criteria and it was suggested by Freudenthal in 1950. He proposed that the beginning of the fracture relates to the plastic work (equivalent stress times equivalent plastic strain) during loading [38]**.** In 1968, Cockroft and Lathmam stated that maximum principle stress has a major role in energy-based fracture, and they replaced the equivalent stress with the maximum principle stress [39]**.** Then, Oh normalized the Cockroft-Latham model by the equivalent stress in 1979 [40]. In addition to Oh's model, in 1984, Ayada normalized the mean stress by the equivalent stress, and therefore, he explained the damage accumulation with stress triaxiality [41]. Similar to Ayada's model, Oyane and Sato added a constant to stress triaxility, and explained fracture with this new function [42].

CHAPTER 3

THEORETICAL BACKGROUND

In this chapter, the theoretical background of the thesis was explained. For this purpose, the theoretical knowledge that was used in this thesis about plasticity, ductile damage, and fatigue, was presented in the following sections.

3.1 Plasticity

Although the structural behavior of many materials in the elastic region is easy to implement in real-life cases, their behavior in the plastic region is not because of their starting point and non-linear stress-strain relation. Therefore, to examine the plastic region of material correctly, a yield criterion and a hardening rule must be used. Moreover, to implement both of them, some main rules and assumptions must be used.

3.1.1 Yield Criterion

When structures are under any combination of loading, a yield criterion determines the point where the elastic deformation finishes and plastic deformation starts. Therefore, it separates the elastic and the plastic regions by creating a limit between them. To perform this, it uses a yield function and data obtained from experiments. Hence, it can be described in closed form as follows:

$$F(\boldsymbol{\sigma}, \boldsymbol{\beta_i}) = 0 \tag{3.1}$$

In this equation, $\boldsymbol{\beta_i}$, $i = 1,2, \dots n$ can be scalar(s), vector(s) or tensor(s) representing expansion, translation and distortion of the yield surface in the stress space. Equation 3.1 represents a general form of yield criteria. These criteria are used for different

material types such as isotropic and orthotropic. For example, von Mises and Tresca yield criteria are used for isotropic materials, Hill48, YLD2003 and BBC2008 yield criteria are used for anisotropic materials. Therefore, an appropriate yield criteria for a given material must be selected for better estimation of yield point. In this thesis, the von Mises yield criteria is used because its simplicity and sufficient representationof the yielding of the materials used.

3.1.1.1 Von-Mises Yield Criteria

Maximum distortion energy criterion or the von Mises criterion states that yielding occurs when the second invariant of deviatoric stress J_2 reaches a critical value K^2 which is a material property and it can be demonstrated as follows:

$$F = J_2 - \text{K}^2 = 0 \tag{3.2}$$

where the second invariant of deviatoric stress can be written as:

$$J_2 = \frac{1}{2}\sigma'_{ij}\sigma'_{ij} \tag{3.3}$$

and σ'_{ij} is the deviatoric stress tensor given by:

$$\sigma'_{ij} = \sigma_{ij} - \frac{1}{3}\delta_{ij}\sigma_{kk} \tag{3.4}$$

Since in general, yielding is independent of hydrostatic stresses except for porous materials [43], to examine yielding, deviatoric stress space which is shown in Equation 3.4 can be used. From a simple tension test, the value of K can found as $\sigma_Y/\sqrt{3}$. Therefore, by using the above relations, von Mises yield criteria can be stated as follows:

$$F = \sqrt{\frac{3}{2}\sigma'_{ij}\sigma'_{ij}} - \sigma_Y = 0 \tag{3.5}$$

When $F < 0$, materials experience elastic deformation, whereas for the plastic deformation of the material $F = 0$. Equation 3.4 can be expressed geometrically as a cylinder in 3D principal stress space which was shown in Figure 3.1. For the plane stress condition, that is, interaction of the cylinder with 2D stress space, an ellipse that defines the von Mises criterion is obtained.

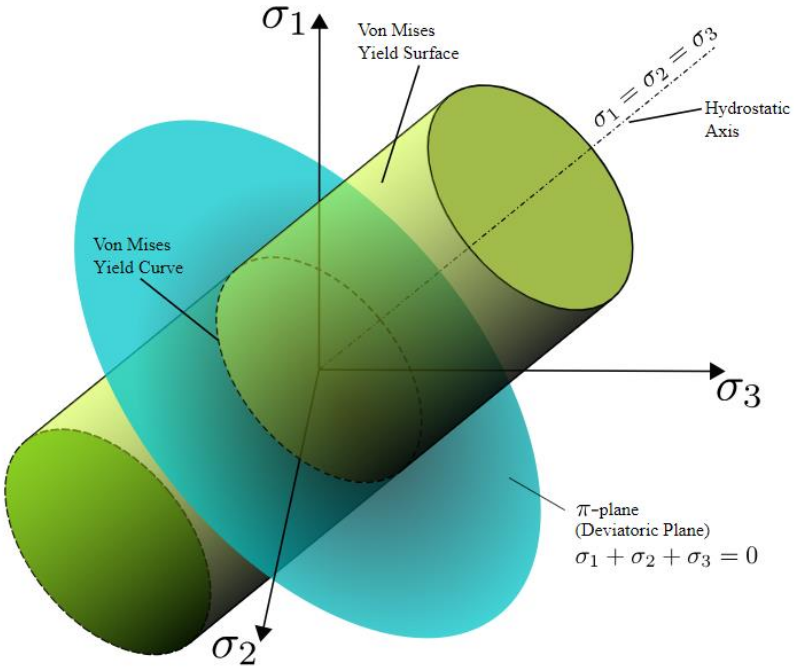

Figure 3.1: Von-Mises Yield Surface in 3D Stress Space [44]

The surface of the cylinder expresses as the yield surface. If the von Mises stress is inside the surface of the cylinder, yielding does not occur. If it is on the yield surface, yielding starts and plastic deformation can continue by any further loading with expansion, translation, or both expansion and translation of the yield surface according to the selected hardening law.

The von Mises stress can be also defined in principal stress space as follows:

$$\bar{\sigma} = \sqrt{\frac{(\sigma_1 - \sigma_2)^2 + (\sigma_1 - \sigma_3)^2 + (\sigma_2 - \sigma_3)^2}{2}} \tag{3.6}$$

Then, by assuming plane stress conditions and thus, taking $\sigma_3 = 0$, von Mises stresses in 2D principal stress space can be obtained as:

$$\bar{\sigma} = \sqrt{\frac{(\sigma_1 - \sigma_2)^2 + (\sigma_1)^2 + (\sigma_2)^2}{2}} \tag{3.7}$$

3.1.1.2 The Normality Hypothesis

The normality hypothesis states that the increment of the plastic strain tensor is perpendicular to the yield surface, as shown in Figure 3.2.

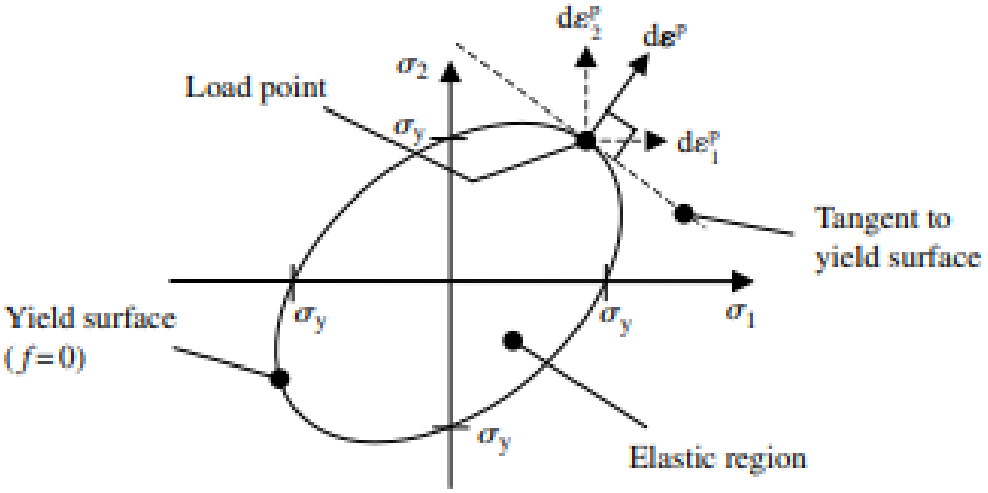

Figure 3.2: Von-Mises Yield Surface (2D) with Normality Hypothesis [45]

The normality hypothesis can be expressed mathematically by using the yield function as follows:

$$d\boldsymbol{\varepsilon^p} = d\lambda \frac{\partial F}{\partial \boldsymbol{\sigma}} \tag{3.8}$$

From Equation 3.8, it can be concluded that while the magnitude of progression of the yield surface is related to the plastic strain rate ($\dot{\lambda}$) or increment ($d\lambda$), its direction is determined by the derivative of yield function with respect to stress tensor ($\partial F/\partial \boldsymbol{\sigma}$).

The term $\partial F/\partial \boldsymbol{\sigma}$ can be found for von Mises Yield criterion by taking the derivative of Equation 3.5 with respect to $\boldsymbol{\sigma}$.

$$\frac{\partial F}{\partial \boldsymbol{\sigma}} = \frac{3}{2}\frac{\boldsymbol{\sigma}'}{\bar{\sigma}} \tag{3.9}$$

Moreover, since equivalent plastic strain increment ($d\bar{\varepsilon}^p$) can be written as:

$$d\bar{\varepsilon}^p = \sqrt{\frac{2}{3} d\boldsymbol{\varepsilon}^{\boldsymbol{p}} : d\boldsymbol{\varepsilon}^{\boldsymbol{p}}} \tag{3.10}$$

The relation between plastic multiplier and equivalent plastic strain can be obtained by putting Equation 3.8 and Equation 3.9 into Equation 3.10 as follows:

$$d\bar{\varepsilon}^p = \sqrt{\frac{2}{3} d\lambda \frac{3}{2}\frac{\boldsymbol{\sigma}'}{\bar{\sigma}} : d\lambda \frac{3}{2}\frac{\boldsymbol{\sigma}'}{\bar{\sigma}}} \tag{3.11}$$

$$d\bar{\varepsilon}^p = \frac{d\lambda}{\bar{\sigma}} \sqrt{\frac{3}{2} \boldsymbol{\sigma}' : \boldsymbol{\sigma}'} \tag{3.12}$$

$$d\bar{\varepsilon}^p = d\lambda \tag{3.13}$$

As a result, it is found that the equivalent plastic strain rate is equal to the plastic multiplier rate.

3.1.1.3 Consistency Condition

For time-independent plasticity, the consistency condition states that during plastic deformation, the stress point remains on the yield surface. This can be expressed for von Mises yield criterion considering strain hardening as follows:

$$F(\boldsymbol{\sigma}, \bar{\varepsilon}^p) = \bar{\sigma} - \sigma_Y = \bar{\sigma}(\boldsymbol{\sigma}) - \sigma_Y(\bar{\varepsilon}^p) = 0 \tag{3.14}$$

$$F(\boldsymbol{\sigma}, \bar{\varepsilon}^p) = F(\boldsymbol{\sigma} + d\boldsymbol{\sigma}, \bar{\varepsilon}^p + d\bar{\varepsilon}^p) = 0 \tag{3.15}$$

From Taylor series expansion:

$$F(\boldsymbol{\sigma} + d\boldsymbol{\sigma}, \bar{\varepsilon}^p + d\bar{\varepsilon}^p) = F(\boldsymbol{\sigma}, \bar{\varepsilon}^p) + \frac{\partial F}{\partial \boldsymbol{\sigma}} \cdot d\boldsymbol{\sigma} + \frac{\partial F}{\partial \bar{\varepsilon}^p} d\bar{\varepsilon}^p \tag{3.16}$$

Hence, Equations 3.14 and 3.15 lead to the following:

$$\frac{\partial F}{\partial \boldsymbol{\sigma}} \cdot d\boldsymbol{\sigma} + \frac{\partial F}{\partial \bar{\varepsilon}^p} d\bar{\varepsilon}^p = 0 \tag{3.17}$$

To solve Equation 3.17, two unkonows which are $d\boldsymbol{\sigma}$ and $d\bar{\varepsilon}^p$ must be examined. Generalized Hooke's Law and strain rate decomposition can be used to find $d\boldsymbol{\sigma}$ as follows:

$$d\boldsymbol{\sigma} = \boldsymbol{C} d\boldsymbol{\varepsilon^e} = \boldsymbol{C}(d\boldsymbol{\varepsilon} - d\boldsymbol{\varepsilon^p}) \tag{3.18}$$

From the normality hypothesis, Equation 3.18 becomes:

$$d\boldsymbol{\sigma} = \boldsymbol{C}\left(d\boldsymbol{\varepsilon} - d\lambda \frac{\partial F}{\partial \boldsymbol{\sigma}}\right) \tag{3.19}$$

In addition, to find $d\bar{\varepsilon}^p$, the definition of equivalent plastic strain and the normality condition can be used and this leads to as following:

$$d\bar{\varepsilon}^p = \sqrt{\frac{2}{3} d\boldsymbol{\varepsilon^p} \cdot d\boldsymbol{\varepsilon^p}} = \sqrt{\frac{2}{3}\left(d\lambda \frac{\partial F}{\partial \boldsymbol{\sigma}}\right) \cdot \left(d\lambda \frac{\partial F}{\partial \boldsymbol{\sigma}}\right)} \tag{3.20}$$

Then, by substituting equations 3.19 and 3.20 into equation 3.17, the following relation can be obtained:

$$\frac{\partial F}{\partial \boldsymbol{\sigma}} \cdot \boldsymbol{C}\left(d\boldsymbol{\varepsilon} - d\lambda \frac{\partial F}{\partial \boldsymbol{\sigma}}\right) + \frac{\partial F}{\partial \bar{\varepsilon}^p}\sqrt{\frac{2}{3}\left(d\lambda \frac{\partial F}{\partial \boldsymbol{\sigma}}\right) \cdot \left(d\lambda \frac{\partial F}{\partial \boldsymbol{\sigma}}\right)} = 0 \tag{3.21}$$

By solving Equation 3.21 for the plastic multiplier, the following relation can be obtained:

$$d\lambda = \frac{\frac{\partial F}{\partial \boldsymbol{\sigma}} \cdot \boldsymbol{C} d\boldsymbol{\varepsilon}}{\frac{\partial F}{\partial \boldsymbol{\sigma}} \cdot \boldsymbol{C} \frac{\partial F}{\partial \boldsymbol{\sigma}} - \frac{\partial F}{\partial \bar{\varepsilon}^p}\sqrt{\frac{2}{3}\frac{\partial F}{\partial \boldsymbol{\sigma}} \cdot \frac{\partial F}{\partial \boldsymbol{\sigma}}}} \tag{3.22}$$

This enables us to find stress values by using an elastoplastic stiffness matrix as follows:

$$d\boldsymbol{\sigma} = \left(\boldsymbol{C} - \frac{\frac{\partial F}{\partial \boldsymbol{\sigma}} \cdot \boldsymbol{C}}{\frac{\partial F}{\partial \boldsymbol{\sigma}} \cdot \boldsymbol{C} \frac{\partial F}{\partial \boldsymbol{\sigma}} - \frac{\partial F}{\partial \bar{\varepsilon}^p}\sqrt{\frac{2}{3}\frac{\partial F}{\partial \boldsymbol{\sigma}} \cdot \frac{\partial F}{\partial \boldsymbol{\sigma}}}} \frac{\partial F}{\partial \boldsymbol{\sigma}}\right) d\boldsymbol{\varepsilon} \tag{3.23}$$

$$d\boldsymbol{\sigma} = \boldsymbol{C_{ep}} d\boldsymbol{\varepsilon} \tag{3.24}$$

Note that, when the plastic multiplier is equal to zero ($d\lambda$), the elastoplastic stiffness matrix is equal to the elastic stiffness matrix ($\boldsymbol{C_{ep}} = \boldsymbol{C}$).

3.1.2 Hardening Rules

After yielding occurs, the amount of stress needed for obtaining plastic deformation increases. This phenomenon is called hardening. The evolution of the yield surface can be obtained with an appropriate hardening rule. There are three basic hardening rules which are isotropic hardening, kinematic hardening, and combined or mixed hardening.

3.1.2.1 Isotropic Hardening Rule

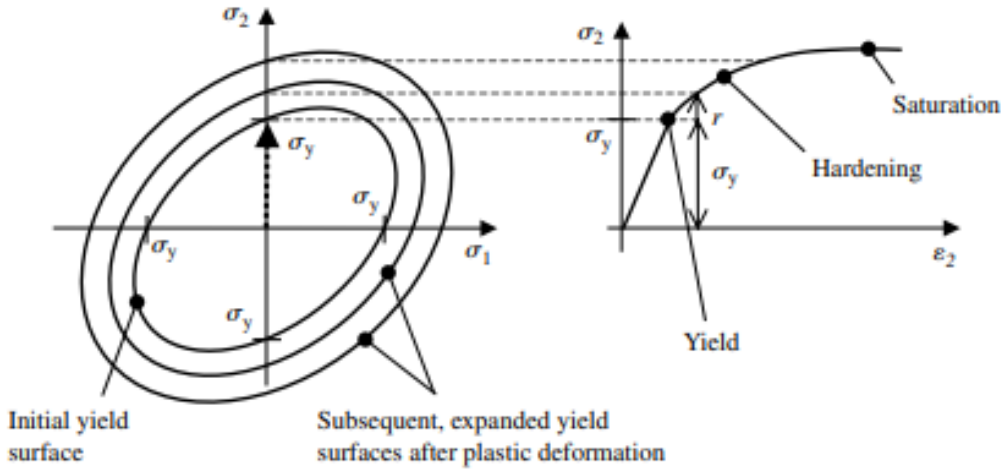

Figure 3.3: Isotropic Hardening [45]

After yielding, when the yield surface of a material expands or shrinks uniformly without any translation, hardening behavior of the material is explained with isotropic hardening. In isotropic hardening yield surface does not move, only its shape changes. Moreover, because of the consistency condition, when it changes its shape, its yield strength also changes as can be seen in Figure 3.3. Hence, its yield strength is dependent on the plastic strain as follows:

$$F(\boldsymbol{\sigma}, \bar{\varepsilon}^p) = \bar{\sigma} - \sigma_Y(\bar{\varepsilon}^p) \tag{3.25}$$

Although there are various isotropic hardening functions, the isotropic part of the Chaboche-Lemaitre model can be written as follows:

$$\sigma_Y(\bar{\varepsilon}^p) = \sigma_{Y0} + Q\left(1 - e^{-b\bar{\varepsilon}^p}\right) \tag{3.26}$$

where σ_{Y0} is the initial yield point without any hardening, Q is the maximum stress value obtained from the saturation point shown in Figure 3.3, and b is the rate of stress for obtaining the saturation point.

As a result of the evolution of the consistency condition and the normality hypothesis, the plastic multiplier can be found as below:

$$d\lambda = \frac{-\frac{\partial F}{\partial \boldsymbol{\sigma}} \cdot d\boldsymbol{\sigma}}{\frac{2}{3}\frac{\partial F}{\partial \boldsymbol{\sigma}}\frac{\partial F}{\partial \bar{\varepsilon}^p} \cdot \frac{\partial F}{\partial \boldsymbol{\sigma}}} \tag{3.27}$$

3.1.2.2 Kinematic Hardening Rule

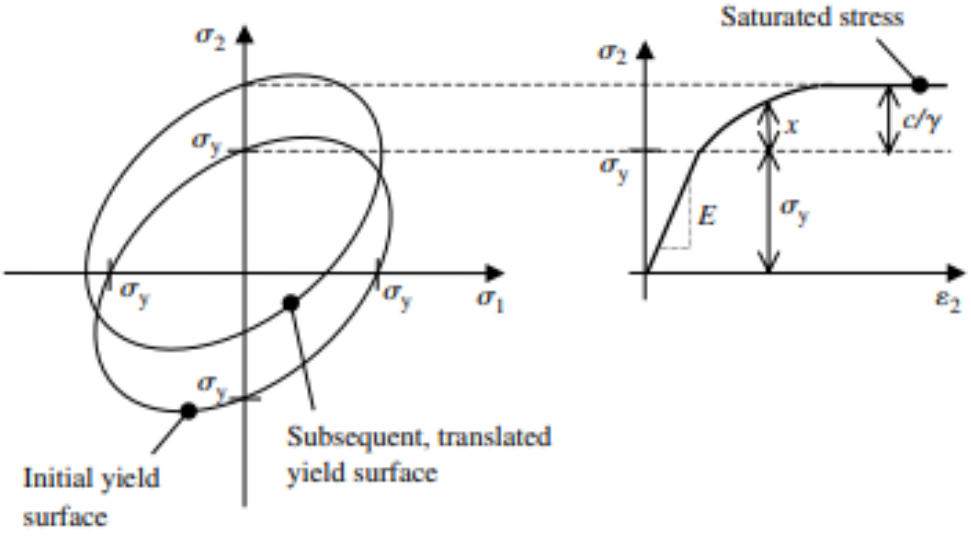

Figure 3.4: Kinematic Hardening [45]

After yielding, when the yield surface translates in stress space without any shape change of the yield surface, hardening behavior of the material is explained with kinematic hardening as shown in Figure 3.4. Since in kinematic hardening, there is only translation for yield surface evolution, the amount of translation is measured by a reference point. For that reason, a reference stress point called back stress ($\boldsymbol{\alpha}$) exists in the yield function as follows:

$$F = f(\boldsymbol{\sigma}' - \boldsymbol{\alpha}) - \sigma_Y = 0 \tag{3.28}$$

For von Mises yield criterion, it can be written as below:

$$F = \sqrt{\frac{3}{2}(\boldsymbol{\sigma}' - \boldsymbol{\alpha})(\boldsymbol{\sigma}' - \boldsymbol{\alpha})} - \sigma_Y = 0 \tag{3.29}$$

where for non-linear kinematic hardening, incremental back stress ($d\boldsymbol{\alpha}$) can be expressed as below:

$$d\boldsymbol{\alpha} = c\frac{d\bar{\varepsilon}_p}{\bar{\sigma}}(\boldsymbol{\sigma}' - \boldsymbol{\alpha}) - \gamma\boldsymbol{\alpha}d\bar{\varepsilon}_p \tag{3.30}$$

where c and γ are the kinematic hardening material constants. These two material constants determine the saturated stress (c/γ) for kinematic hardening shown in Figure 3.4.

By using the normality hypothesis, and consistency condition, the plastic multiplier for the kinematic hardening can be found as follows:

$$d\lambda = \frac{-\frac{\partial F}{\partial \boldsymbol{\sigma}} \cdot d\boldsymbol{\sigma}}{\gamma\frac{\partial F}{\partial \boldsymbol{\sigma}} \cdot \boldsymbol{\alpha} - \frac{2}{3}c\frac{\partial F}{\partial \boldsymbol{\sigma}} \cdot \frac{\partial F}{\partial \boldsymbol{\sigma}}} \tag{3.31}$$

3.1.2.3 Comparison between Isotropic and Kinematic Hardening

Although in monotonically increasing loading, isotropic and kinematic hardening give close results with respect to each other, when reverse loading occurs the results differ from each other. As it is seen in Figure 3.5, when reverse loading occurs, yield strength values at compression and tension are the same in isotropic hardening. However, by examining Figure 3.6, it can be seen that during kinematic hardening, the yield strength in compression is smaller than the yield strength in tension or vice versa. This phenomenon is called Bauchinger's effect, and makes the kinematic hardening more reliable than the isotropic hardening for cyclic loading cases.

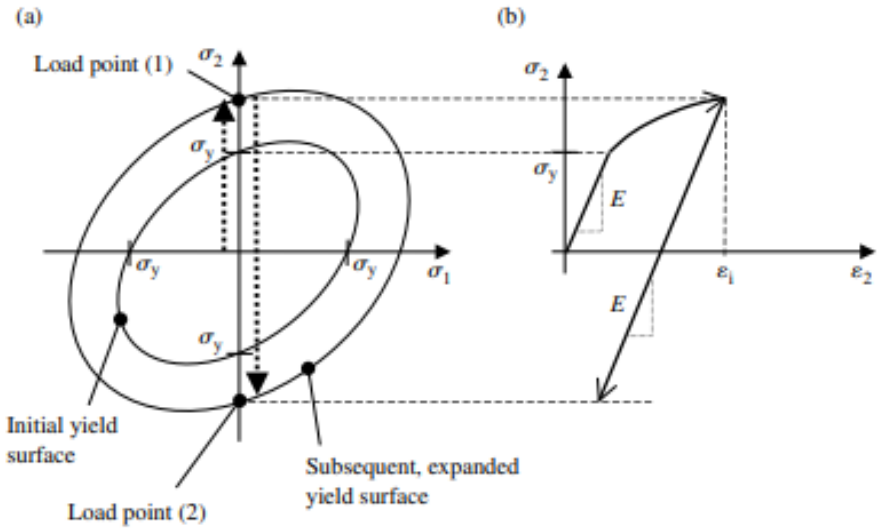

Figure 3.5: Isotropic Hardening under Reverse Loading [45]

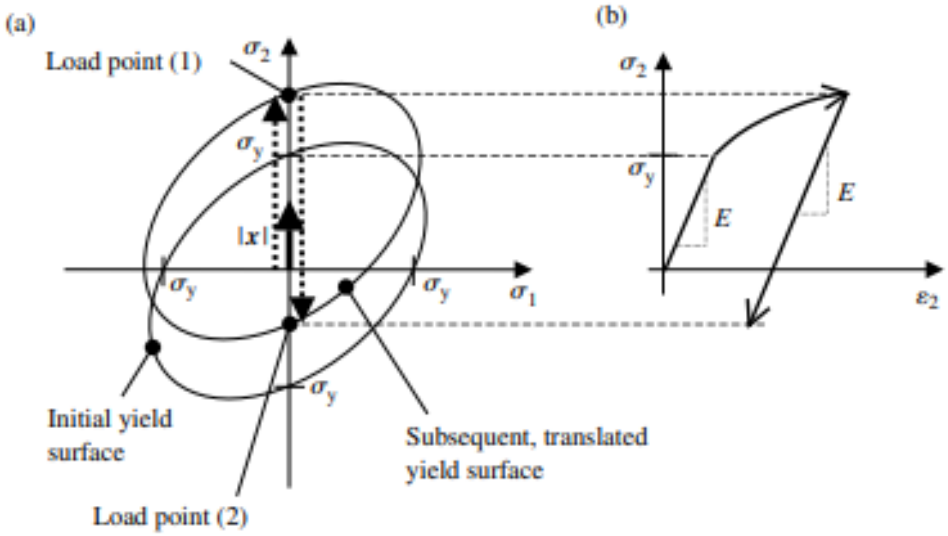

Figure 3.6: Kinematic Hardening under Reverse Loading [45]

3.1.2.4 Combined Hardening Rule

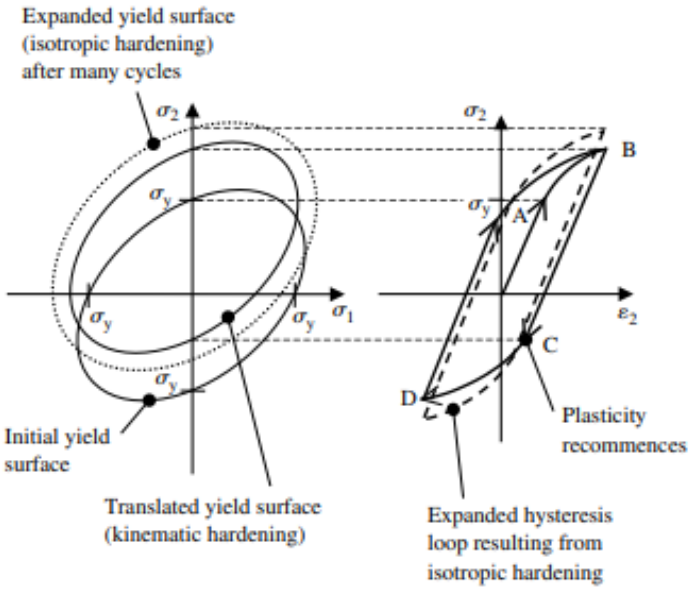

Figure 3.7: Combined Hardening [45]

So far it has been discussed that the yield surface of a material expands by isotropic hardening or translates by kinematic hardening. Although they were examined separately, they can be revealed in a structure together by combined hardening. In combined hardening, the yield surface of a material both expands and translates. Therefore, it covers the Baushinger effect. Although in combined hardening, most of the contribution results from the kinematic hardening, after many cycles, isotropic hardening gains importance on the evolution of yield surface [45]. The yield function of the combined hardening can be expressed as follows:

$$F = f(\boldsymbol{\sigma}' - \boldsymbol{\alpha}) - \sigma_Y(\bar{\varepsilon}^p) \tag{3.32}$$

where $\sigma_Y(\bar{\varepsilon}^p)$ is isotropic part and stated in Equation 3.26. Moreover, the consistency equation becomes,

$$\frac{\partial F}{\partial \boldsymbol{\sigma}} \cdot d\boldsymbol{\sigma} + \frac{\partial F}{\partial \boldsymbol{\alpha}} \cdot d\boldsymbol{\alpha} + \frac{\partial F}{\partial \bar{\varepsilon}^p} d\bar{\varepsilon}^p = 0 \tag{3.33}$$

By considering the normality hypothesis and consistency equation, the plastic multiplier can be found as follows:

$$d\lambda = \frac{\frac{\partial F}{\partial \boldsymbol{\sigma}} \cdot d\boldsymbol{\sigma}}{\frac{2}{3} c \frac{\partial F}{\partial \boldsymbol{\sigma}} \cdot \frac{\partial F}{\partial \boldsymbol{\sigma}} - \gamma \frac{\partial F}{\partial \boldsymbol{\sigma}} \cdot \boldsymbol{\alpha} + Qbe^{-b\bar{\varepsilon}^p}} \tag{3.34}$$

3.1.3 Radial Return Method

During explicit finite element analysis, the evolution of stress, plastic strain, and yield strength can be expressed by the following equations:

$$^{t+\Delta t}\sigma = {}^{t}\sigma + \Delta^{t}\sigma \tag{3.35}$$

$$^{t+\Delta t}\varepsilon^{p} = {}^{t}\varepsilon^{p} + \Delta^{t}\varepsilon^{p} \tag{3.36}$$

$$^{t+\Delta t}(\sigma_Y) = {}^{t}(\sigma_Y) + \Delta^{t}(\sigma_Y) \tag{3.37}$$

These numerical equations can be explained with the first-order forward Euler method. The main disadvantage of this method for plasticity is that although it satisfies the yield condition at time t, it does not ensure the satisfaction of the yield condition at time $t + \Delta t$ since it does not ensure the location of the stress point in the yield surface at time $t + \Delta t$. For that reason, by adding an implicit behavior, the Radial Return Method can be used to move the stress point on the yield surface.

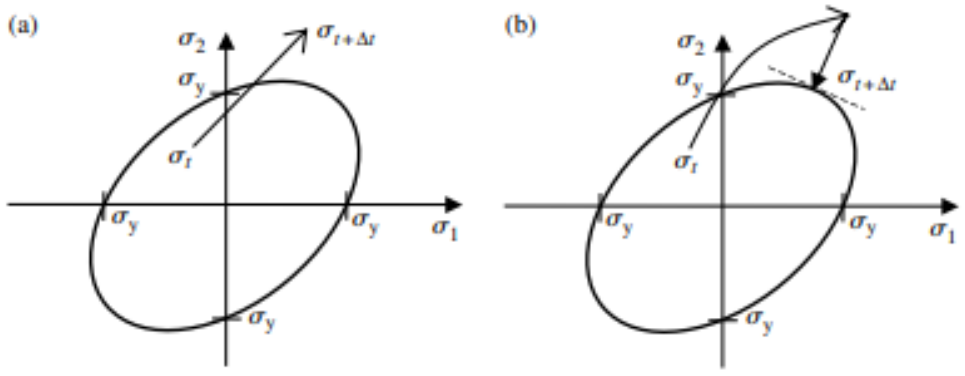

Figure 3.8: Radial Return Method (a) Explicit Integration (b) Implicit Integration [45]

The Radial Return Method includes two parts which are explicit integration and implicit integration, shown in Figure 3.8. In the explicit integration part, a forward Euler method is used to predict stress at time $t + \Delta t$, and this prediction is made pure elastically. Then, in the implicit integration part, for the yield surface is checked and by using a plastic corrector, stress is projected to the yield surface.

To explain elastic predictor and plastic corrector, using Hooke's Law:

$$\boldsymbol{\sigma} = 2G\boldsymbol{\varepsilon}^e + \lambda tr(\boldsymbol{\varepsilon}^e)\boldsymbol{I} \tag{3.38}$$

and decomposition of elastic strain tensor $\boldsymbol{\varepsilon}^e$:

$$\boldsymbol{\varepsilon}^e = \boldsymbol{\varepsilon}_t^e + \Delta\boldsymbol{\varepsilon}^e = \boldsymbol{\varepsilon}_t^e + \Delta\boldsymbol{\varepsilon} - \Delta\boldsymbol{\varepsilon}^p \tag{3.39}$$

Equation 3.38 can be written as:

$$\boldsymbol{\sigma} = 2G(\boldsymbol{\varepsilon}_t^e + \Delta\boldsymbol{\varepsilon} - \Delta\boldsymbol{\varepsilon}^p) + \lambda tr(\boldsymbol{\varepsilon}_t^e + \Delta\boldsymbol{\varepsilon} - \Delta\boldsymbol{\varepsilon}^p)\boldsymbol{I} \tag{3.40}$$

By using constant volume assumption in the plastic region, that is $tr(\Delta\boldsymbol{\varepsilon}^p) = 0$

$$\boldsymbol{\sigma} = 2G(\boldsymbol{\varepsilon}_t^e + \Delta\boldsymbol{\varepsilon}) + \lambda tr(\boldsymbol{\varepsilon}_t^e + \Delta\boldsymbol{\varepsilon})\boldsymbol{I} - 2G\Delta\boldsymbol{\varepsilon}^p \tag{3.41}$$

Equation 3.41 includes both elastic predictor and plastic corrector. In this equation, elastic predictor or trial stress in explicit integration is expressed as:

$$\boldsymbol{\sigma}^{tr} = 2G(\boldsymbol{\varepsilon}_t^e + \Delta\boldsymbol{\varepsilon}) + \lambda tr(\boldsymbol{\varepsilon}_t^e + \Delta\boldsymbol{\varepsilon})\boldsymbol{I} \tag{3.42}$$

whereas, plastic corrector is

$$\boldsymbol{\sigma}^{corrector} = -2G\Delta\boldsymbol{\varepsilon}^p \tag{3.43}$$

3.2 Fatigue Failure

Repeating loads that cause stresses lower than yield strength or ultimate strength can result in fracture. This phenomenon is called fatigue failure. The fatigue failure has three main stages which are crack initiation, propagation, and fracture which can be shown in Figure 3.9. For the prediction of crack initiation, stress, strain, or energy-based methods are used. Moreover, for crack propagation prediction, fracture mechanics is used.

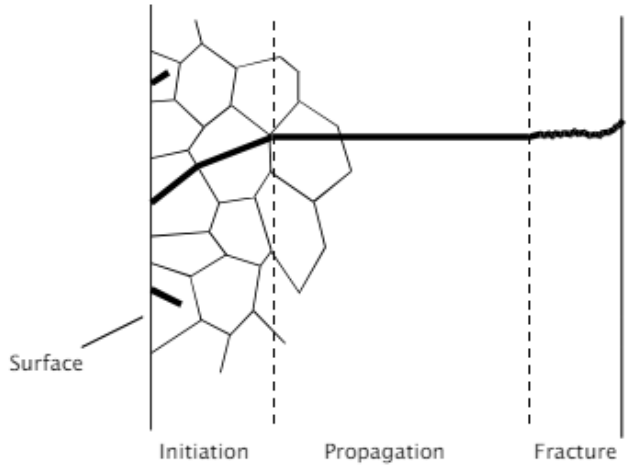

Figure 3.9: Three Stages of Fatigue Failure [46]

Fatigue failures are classified by low-cycle fatigue and high-cycle fatigue. Although there are various limits proposed by many resources, in general, when the number of cycles to failure is smaller than 1000, it is called low-cycle fatigue, and if it is higher than that value, it is called high-cycle fatigue. The strain life methods are preferred for low-cycle fatigue, stress life methods are used for high-cycle fatigue. In addition, energy-based methods can be used for both of low and high cycle cases. Since the properties of the cycle have a major role in the fatigue life, their effect must also be evaluated. The cycle can be summarized by its range, amplitude, mean, etc. induced by either load, stress, or strain. A load-cycle is presented in Figure 3.10, and related equations are given below:

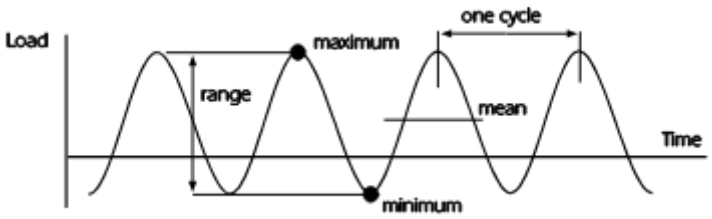

Figure 3.10: Analysis of Cyclic Loading [46]

Stress range:

$$\Delta\sigma = \sigma_{max} - \sigma_{min} \tag{3.44}$$

Stress amplitude:

$$\sigma_A = \frac{\Delta\sigma}{2} \tag{3.45}$$

Mean stress:

$$\sigma_M = \frac{\sigma_{max} + \sigma_{min}}{2} \tag{3.46}$$

Stress ratio:

$$R = \frac{\sigma_{min}}{\sigma_{max}} \tag{3.47}$$

Amplitude ratio:

$$A = \frac{\sigma_A}{\sigma_M} \tag{3.48}$$

3.3 Fracture

Under the necessary amount of stress, molecular bonds in materials can be broken and this creates two surfaces between these broken molecular bonds. This phenomenon is called fracture. Fracture is the final stage of the plastic deformation for ductile materials, and it is crucial for all engineering materials. Fractures can be classified into two main categories which are brittle and ductile fractures. The main difference between them is the amount of plastic deformation exposed until fracture. In brittle fracture, materials experience a very little plastic deformation whereas, in ductile fracture, materials encounter a large amount of plastic deformation.

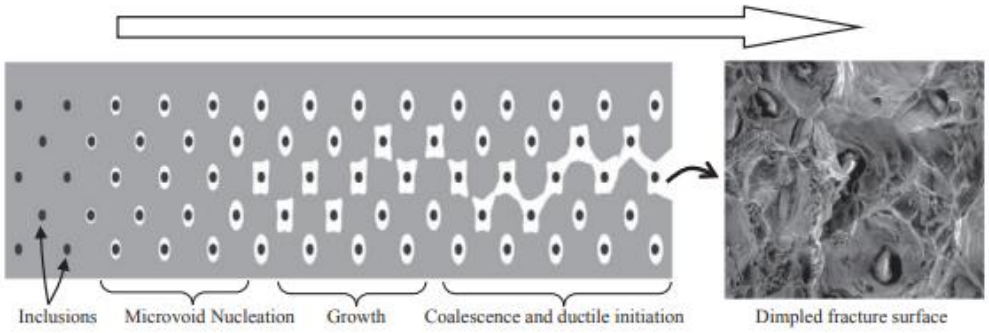

Figure 3.11: Ductile Fracture Initiation [47]

As is seen in Figure 3.11, the growth and coalescence of microvoids around inclusions result in ductile fracture. Ductile fracture can occur in different manners under various loading conditions. This situation makes ductile fracture prediction difficult. Various ductile criteria have been suggested to predict ductile fracture initiation under different loading conditions. These ductile fracture criteria (DFCs) can be examined in two categories: Coupled DFCs and Uncoupled DFCs.

3.3.1 Coupled Ductile Fracture Criteria (CDFC)

Coupled Ductile Fracture Criteria (CDFC) determine damage accumulation by including the related equations in the constitutive equations and modifying the yield surface with the change of damage. The most popular CDFCs are the continuum damage mechanics (CDM) model which explains damage as the void density in structure, and Gurson-Tvergaard-Needleman (GTN) model which considers damage as void volume fraction. Changing yield surface by damage makes it necessary to implement these criteria in the FEM codes.

3.3.2 Uncoupled Ductile Fracture Criteria (UDFC)

Uncoupled Ductile Fracture Criteria (UDFC) formulate damage accumulation empirically or semi-empirically with a general function. This general function which is given with the following equation can be formulated by using numerical and experimental observations and their combinations.

$$\int_0^{\bar{\varepsilon}_f} f(\boldsymbol{\sigma}, \bar{\varepsilon}^p) d\bar{\varepsilon}^p \geq C \tag{3.49}$$

Here, $\boldsymbol{\sigma}$ is the Cauchy stress tensor, $\bar{\varepsilon}^p$ is the equivalent plastic strain, $\bar{\varepsilon}_f$ is the equivalent plastic strain at fracture, and C is data determined by experimental tests such as uniaxial tensile, shear, biaxial tensile, etc.

Although there are many UDFCs, in this thesis, five of them are used to evaluate the fatigue failure. The first UDFC was put forward by Freudenthal, and it stated that fracture occurs when the sum of the plastic work which is the area under the equivalent stress and equivalent plastic strain ($\bar{\sigma} - \bar{\varepsilon}^p$) during loading reaches a specific value [38] as follows:

$$\int_0^{\bar{\varepsilon}_f} \bar{\sigma} d\bar{\varepsilon}^p \geq C_{FR} \tag{3.50}$$

Cockroft and Latham stated that fracture arises when the maximum principal stress $(\sigma_1)_{max}$ reaches a specific value [39] and it can be expressed by the following equation:

$$\int_0^{\bar{\varepsilon}_f} (\sigma_1)_{max} d\bar{\varepsilon}^p \geq C_{CL} \tag{3.51}$$

Ayada et. al. proposed that fracture depends linearly on stress triaxiality which is the ratio of mean stress ($\sigma_m = \sigma_{kk}/3$) to equivalent stress ($\bar{\sigma}$) [41] as follows:

$$\int_0^{\bar{\varepsilon}_f} \frac{\sigma_m}{\bar{\sigma}} d\bar{\varepsilon}^p \geq C_A \tag{3.52}$$

Oyane and Sato remarked also that the occurrence of the fracture relates to the stress triaxiality [42], however in a different manner, and this relationship can be given as follows:

$$\int_0^{\bar{\varepsilon}_f} \left(\frac{\sigma_m}{\bar{\sigma}} + \frac{1}{3}\right) d\bar{\varepsilon}^p \geq C_{OS} \tag{3.53}$$

Oh. Et. al. proposed that fracture relates to the ratio of maximum principal stress to equivalent stress [40] as below:

$$\int_0^{\bar{\varepsilon}_f} \frac{(\sigma_1)_{max}}{\bar{\sigma}} d\bar{\varepsilon}^p \geq C_O \tag{3.54}$$

CHAPTER 4

FINITE ELEMENT METHOD

4.1 Theoretical Background

4.1.1 An Overview of the Method

Although some basic structural engineering problems can be solved by analytical methods such as the beam theory, the theory of plates, the classical lamination theory, etc., analytical methods become inadequate when a problem includes complex geometry or loading. Therefore, numerical methods can be used for these cases, and there are three main numerical methods which are the finite difference method, the finite element method, and the boundary integral method. Among these methods, the finite element method (FEM) is the most common one for structural analysis applications. The finite element method solves the problems by splitting the body being analyzed into a finite number of elements that are connected with each other by nodes. The sum of all nodes and elements is called a mesh. According to the modeling technique, the element type in the mesh can change. These element types can be line elements, surface elements, or solid elements. Line elements are used for modeling structures such as rods and beams, whereas surface elements are used for modeling structures like thin shells and plates, and finally, solid elements are used for modeling bulk structures. The selection of element type affects directly accuracy and solution time for a problem. In addition to element type, the number of elements in a mesh also affects accuracy and solution time. As the number of elements in a mesh increases, accuracy and solution time increases. Therefore an optimum element size must be selected for an acceptable error and shorter solution time.

4.1.2 Implicit versus Explicit Problems

The selection of a proper finite element analysis (FEA) approach has a major role in the accuracy of the results and efficiency of the analysis. As one of these, finite element analysis can be carried out by implicit and explicit methods. As can be seen in Figure 4.1, the implicit method is more suitable for solving static systems, whereas the explicit method is more suitable for dynamic systems. In addition, for quasi-static problems such as the metal forming process, either implicit or explicit methods can be used.

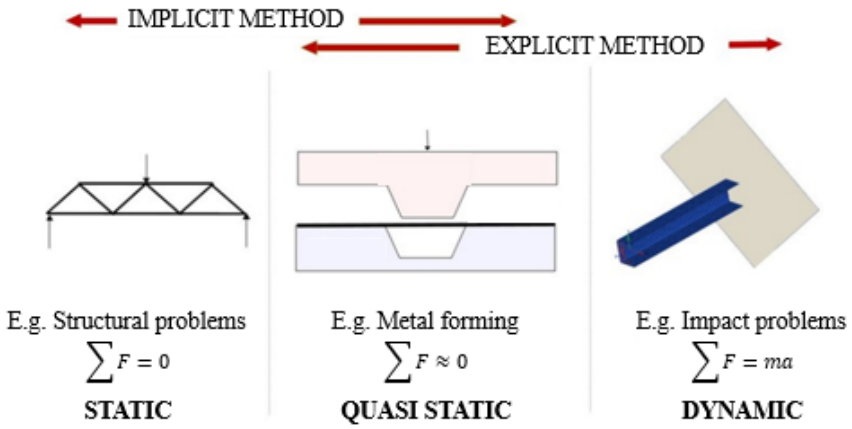

Figure 4.1: FEA Methods for Different Loading Types [48]

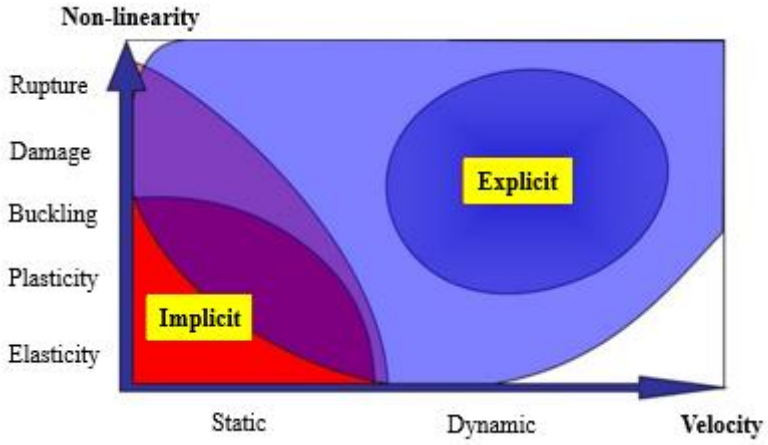

Figure 4.2: Effects of Nonlinearity and Velocity on FEA Method Usage [48]

As can be seen in Figure 4.2, for dynamic analysis where velocity has high values explicit analysis more appropriate. On the other hand, as the nonlinearity of the system increases, so does the usability of explicit analysis. Therefore, velocity and nonlinearity are the two main parameters for choosing implicit or explicit analysis. Although both of these methods solve the following equation their approaches are different.

$$[M]\{u''\} + [C]\{u'\}+[K]\{u\} = \{f\} \tag{4.1}$$

In implicit analysis, Equation 4.1 is solved for displacement value, and for this, as seen below, the inverse of the stiffness matrix is taken. During this operation, the displacement values of both the current and the later iteration are used.

$$\{u\} = [K]^{-1}(\{f\} - [M]\{u''\} - [C]\{u'\}) \tag{4.2}$$

On the other hand, in the explicit analysis, Equation 4.1 is solved for acceleration value, and for this, as seen below, the inverse of the mass matrix is taken.

$$\{u''\} = [M]^{-1}(\{f\} - [C]\{u'\} - [K]\{u\}) \tag{4.3}$$

This operation calculates the later-stage result from the current stage. In most structural problems, mass matrices are diagonal matrices, therefore, they are easy to take inverse. However, compared to mass matrices, stiffness matrices are not diagonal and the number of null elements is not high. For that reason, taking up the inverse of the stiffness matrix increases the storage requirements and solution time. In addition to inverting operation, convergence of an increment also increases the solution time and storage. In implicit analysis, the main goal in each increment is making residual force, that is the difference between external and internal forces, zero. Therefore, to perform this, in each increment, enough number of iterations is solved to obtain a convergent residual force result. On the other hand, in the explicit analysis, the convergence condition is not used. However, the number of iterations is severely higher. As a result, explicit analysis can be preferred in cases where the nonlinearity and dynamic effects are high, and implicit analysis must be preferred in cases where the linearity and static effects are high shown in Figure 4.3.

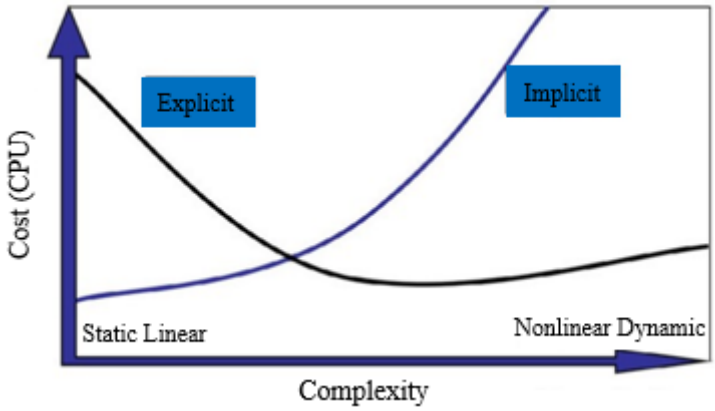

Figure 4.3: Cost Relation of Implicit and Explicit Method [48]

4.1.3 Dynamic Explicit Method

In this thesis, the dynamic explicit FEM was used for the following reasons:

- Analyses with high frequencies were performed.
- The duration of fatigue analyses is long. Therefore, the convergence in each iteration makes the analysis cumbersome.
- For the onset of necking prediction, the stress wave propagation method, which will be discussed in the following chapters, was used.

4.1.3.1 Solution Methodology

During dynamic explicit analysis, the central difference method is used with the equations of motion to calculate acceleration, velocity, and displacement for finding stress and strain values. The methodology can be explained as follows:

- Step 1: Calculate acceleration by the central difference of external and internal forces.

$$ {}^{t}\ddot{u} = \frac{{}^{t}f_{ext} - {}^{t}f_{int}}{m} \tag{4.4} $$

- Step 2: Calculate velocity and displacement values by the Forward Euler method.

$$^{t+\Delta t/2}\dot{u} = {}^{t-\Delta t/2}\dot{u} + {}^{t}\ddot{u}\Delta t \tag{4.5}$$

$$^{t+\Delta t}u = {}^{t}u + {}^{t+\Delta t/2}\dot{u}\Delta t \tag{4.6}$$

- Step 3: Calculate strain and stress values by using their definitions.

$$^{t+\Delta t}\varepsilon = \frac{^{t+\Delta t}u_2 - {}^{t+\Delta t}u_1}{l_0} - 1 \tag{4.7}$$

$$^{t+\Delta t}\sigma = {}^{t+\Delta t}\varepsilon E \tag{4.8}$$

- Step 4: Calculate the internal resultant force by using each nodal force.

$$^{t+\Delta t}f_j = {}^{t+\Delta t}\sigma A_j \tag{4.9}$$

$$^{t+\Delta t}f_{int} = \sum_j {}^{t+\Delta t}f_j \tag{4.10}$$

- Step 5: Calculate acceleration for the new increment

$$^{t+\Delta t}\ddot{u} = \frac{^{t+\Delta t}f_{ext} - {}^{t+\Delta t}f_{int}}{m} \tag{4.11}$$

- Step 6: Repeat steps 1 to 5 until total time is achieved.

4.1.3.2 Stability Condition

Whereas implicit methods are unconditionally stable, explicit methods are conditionally stable. The condition for stability is that the time increment must be smaller than the critical time increment.

$$\Delta t < t_{critical} = \frac{l_e}{c_w} = \frac{l_e}{\sqrt{\frac{E}{\rho}}} \tag{4.12}$$

where c_w is the speed of the wave and depends on material properties which are elastic modulus E and density ρ. Moreover, l_e is the characteristic length of the smallest element in the mesh, and it can be found as follows:

$$l_e = \sqrt[3]{\text{the volume of the smallest element}} \tag{4.13}$$

4.1.3.3 Stress Wave Propagation Method for Necking Prediction

The dynamic explicit solver uses the stress wave propagation method for calculating stress values at each node. It used the wave equation which can be stated as:

$$\rho \frac{\partial^2 u}{\partial t^2} = c_w^2 \frac{\partial^2 u}{\partial x^2} \tag{4.14}$$

where u is the displacement, ρ is the density, and c_w is the wave speed. To solve this equation in FEM, elastic wave speed c_e and plastic wave speed c_p must be calculated:

$$c_e = \sqrt{\frac{E}{\rho}} \tag{4.15}$$

$$c_p = \sqrt{\frac{\frac{d\bar{\sigma}}{d\bar{\varepsilon}}}{\rho}} \tag{4.16}$$

In addition to these speeds, deformation speed during loading is calculated as below:

$$v = \frac{du}{dt} \tag{4.17}$$

Equations 4.15 and 4.16 show that whereas elastic speed is constant during loading, plastic speed changes with the derivative of the equivalent stress with respect to the equivalent strain. Since plastic slope decreases during loading, plastic wave speed decreases too. On the other hand, deformation speed increases when the loading continues. Therefore, plastic wave speed and deformation speed intersect at a specific point as seen in

Figure 4.4, and this point determines the onset of necking in the FEM [49].

Before the intersection point, there is enough time for the propagation of plastic deformation in the gage area of a simple tension test since the plastic wave speed is higher than the deformation speed. Therefore, all the elements in the gage section

have a uniform strain. However, after the intersection point, the deformation speed exceeds the plastic wave speed and this makes some elements reach higher strain than their neighboring elements since neighboring elements delay to obtain high strain values. Therefore, strain values are localized in these elements where the onset of necking is observed in the following figure.

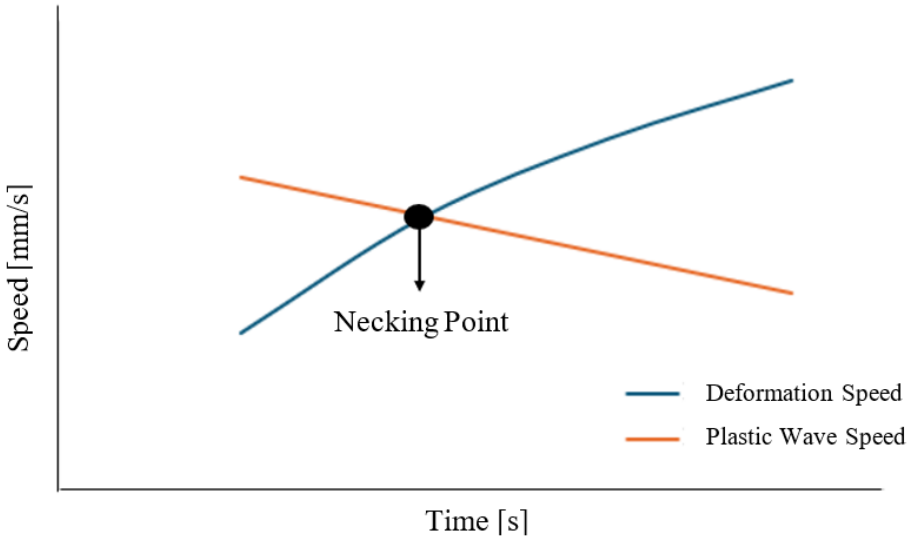

Figure 4.4: Necking Point by Deformation and Plastic Wave Speeds [49]

4.1.3.4 Speeding Up the Dynamic Explicit Problems

Although dynamic explicit analysis is a powerful method for solving many engineering problems, for analyses whose duration is long such as fatigue analyses, it may be necessary to apply some techniques to reduce analysis time. In this case, speeding-up techniques can be used without major changes in results. For this purpose following techniques can be used:

- *Mass Scaling*

An increase in the stable time increment decreases the solution duration. From Equation 4.13, it is seen that when the density of the material increases or the elastic modulus of the material decreases, stable time increment increases and solution time decreases. Since the elastic modulus affects the constitutive relation of a material,

changing it to speed up results in an incorrect solution. However, changing the density is not as critical as elastic modulus. Therefore, changing the density by mass scaling is commonly used to speed up the solution, especially for quasi-static loading. When the speed of the problem increases, mass scaling can affect the accuracy of the results. Therefore, for fatigue analyses, mass scaling was not used.

- *Time Scaling*

Decreasing the total time reduces the number of iterations for a specific stable time increment. In the time scaling method, total time is scaled to a smaller value, so that the solution time decreases. However, decreasing total time results in the increase of loading rate and this is not suitable for rate-dependent cases. In this work, this method was not used since the effect of strain rate is also investigated for critical fatigue life.

- *Reducing output request*

Although analysis is performed in all steps, taking results from all steps increases the time and storage. Hence, the only needed results must be taken from enough amount of intervals to see the behavior of the material clearly. In this thesis, stress, strain, force, displacement, and UDFC constants were requested, and the interval for recording was selected according to the loading rate.

- *Using more processor*

Increasing the number of processors of computers decreases solution time. Hence, the maximum processor capacity in the computer can be selected to reduce the solution time. For this work, a computer having a maximum of 4 processors was used at full capacity to reduce the amount of time for the solution.

- *Avoiding too small local mesh*

Since the stable time increment depends on the minimum characteristic length of a mesh, even only one local element which is smaller than the intended element size

results in a longer solution time. In this thesis, the smallest element size was used in the gage region of the specimen, and locally small meshes were avoided.

- *Reducing the number of elements in the unnecessary portion*

Since increase in the number of elements in mesh results in an increase in the solution time, the portions which are not critical are better to contain fewer elements compared to critical areas. Therefore, in this work, the end sections of the specimen meshed with fewer elements since they are not critical for failure.

4.1.3.5 User Subroutines

In this thesis, although there are many user-defined subroutines in ABAQUS software, the VUMAT subroutine was used since dynamic explicit analyses were performed. The relation of the VUMAT subroutine with ABAQUS software can be seen in Figure 4.5. During these analyses, stress values were calculated in VUMAT to give input for ABAQUS. By using stress values, ABAQUS calculates displacement, velocity, and force values and gives strain as input for VUMAT. This cycle continues until the solution time is completed.

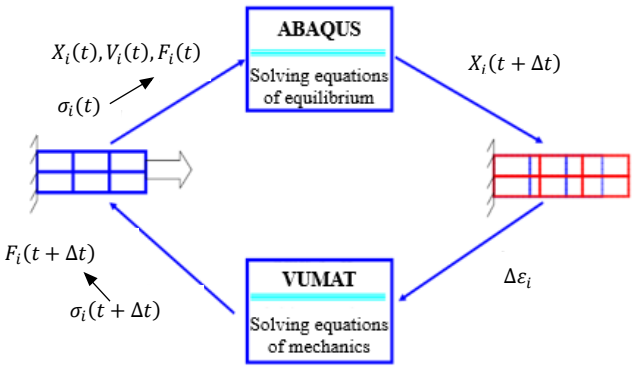

Figure 4.5: ABAQUS and VUMAT Relation [50]

4.2 Finite Element Model

To perform the finite element analysis, the finite element model of the tested specimen was prepared for tensile and fatigue simulations.

4.2.1 Mesh Properties

In this thesis, mesh sensitivity analysis was performed to determine the minimum appopriate number of elements in the gage section of the specimen using the equivalent strain values. As it is seen in Figure 4.6 when the number of elements in the gage section is higher than 2500 elements approximately, the equivalent stress value converges. As a result, 2580 elements were used in the gage section of the finite element model, and it is shown in Figure 4.7. The approximate element size in the gage section is 1.33 mm, and the type of element is C3D8R (an 8-node linear brick, reduced integration, hourglass control).

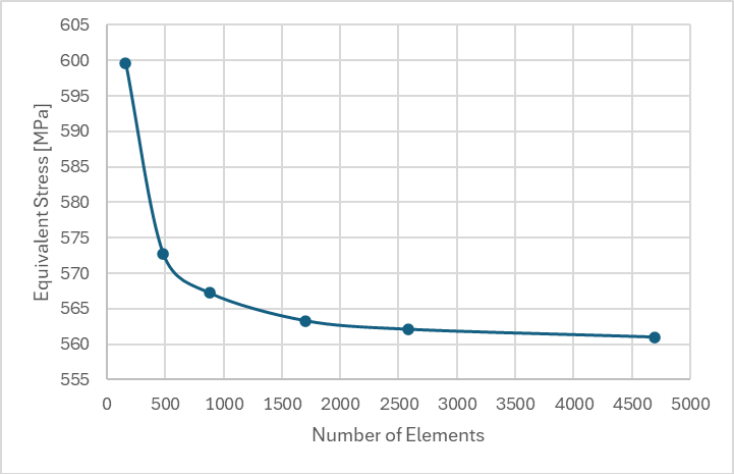

Figure 4.6: Equivalent Stress vs. Number of Elements in Gage Section

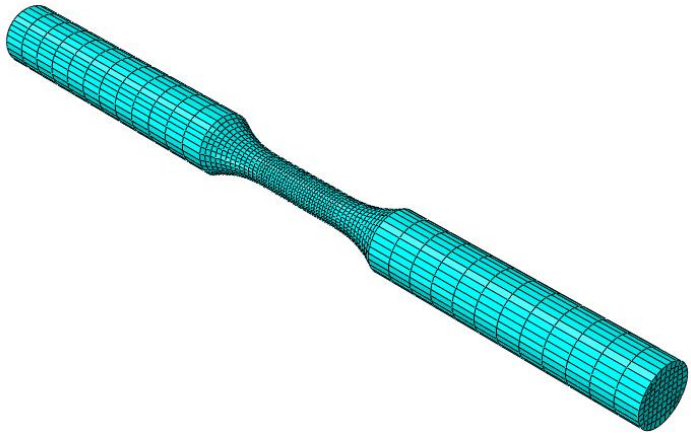

Figure 4.7: Finite Element Model of the Specimen

4.2.2 Load and Boundary Conditions

In the finite element model used in this study, shown in Figure 4.8, a concentrated force was applied to one of the ends of the specimen by means of kinematic coupling and the other was fixed at the other end connection. In addition, to avoid displacement other than the loading direction, at the point where the force applied, displacements other than the loading direction were not allowed.

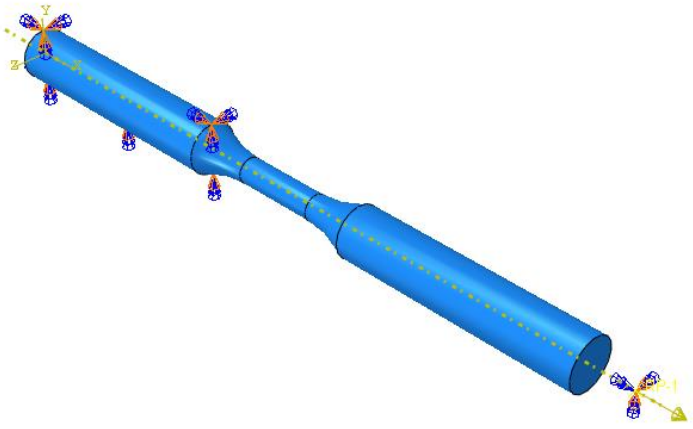

Figure 4.8: Load and Boundary Condition

4.2.3 VUMAT Code Algorithm

A VUMAT subroutine was written to calculate UDFC constants in all performed simulations. The algorithm of this subroutine can be shown as follows:

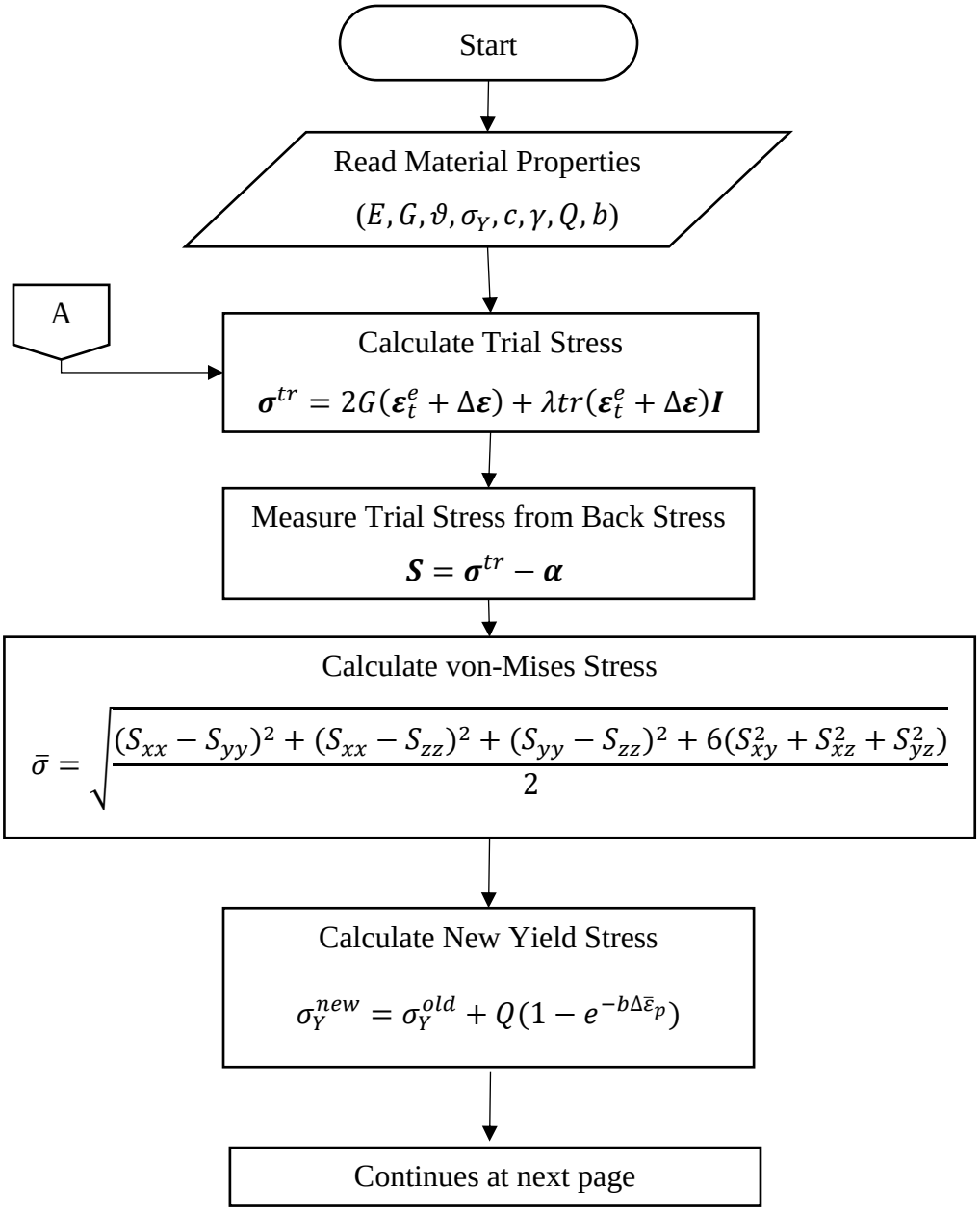

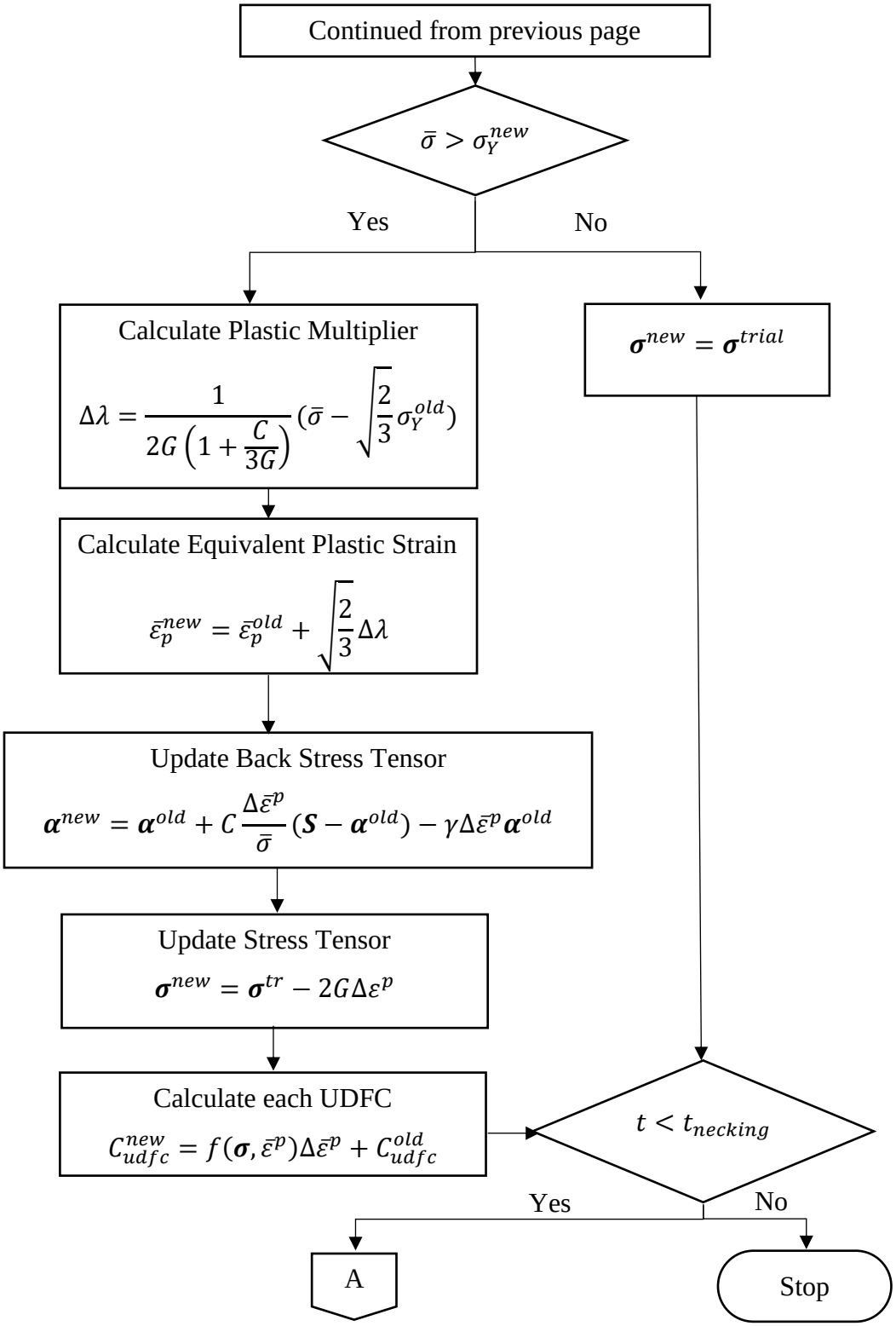
Continued from previous page
$\bar{\sigma} > \sigma_Y^{new}$
Yes
No
Calculate Plastic Multiplier
$\Delta\lambda = \frac{1}{2G\left(1+\frac{C}{3G}\right)}(\bar{\sigma} - \sqrt{\frac{2}{3}}\sigma_Y^{old})$
$\boldsymbol{\sigma}^{new} = \boldsymbol{\sigma}^{trial}$
Calculate Equivalent Plastic Strain
$\bar{\varepsilon}_p^{new} = \bar{\varepsilon}_p^{old} + \sqrt{\frac{2}{3}}\Delta\lambda$
Update Back Stress Tensor
$\boldsymbol{\alpha}^{new} = \boldsymbol{\alpha}^{old} + C\frac{\Delta\bar{\varepsilon}^p}{\bar{\sigma}}(\boldsymbol{S} - \boldsymbol{\alpha}^{old}) - \gamma\Delta\bar{\varepsilon}^p\boldsymbol{\alpha}^{old}$
Update Stress Tensor
$\boldsymbol{\sigma}^{new} = \boldsymbol{\sigma}^{tr} - 2G\Delta\varepsilon^p$
Calculate each UDFC
$C_{udfc}^{new} = f(\boldsymbol{\sigma}, \bar{\varepsilon}^p)\Delta\bar{\varepsilon}^p + C_{udfc}^{old}$
$t < t_{necking}$
Yes
No
A
Stop

CHAPTER 5

EXPERIMENTS

5.1 Test Properties

In this thesis, specimens made from AISI4140 steel were tested under uniaxial tensile force. The dimensions of the specimens can be shown in Figure 5.1. The tests were conducted by using the DARTEC universal testing machine which is shown in Figure 5.2 with a constant velocity of 0.05 mm/s. The force and displacement values were recorded by machine and strain values were recorded by an extensometer.

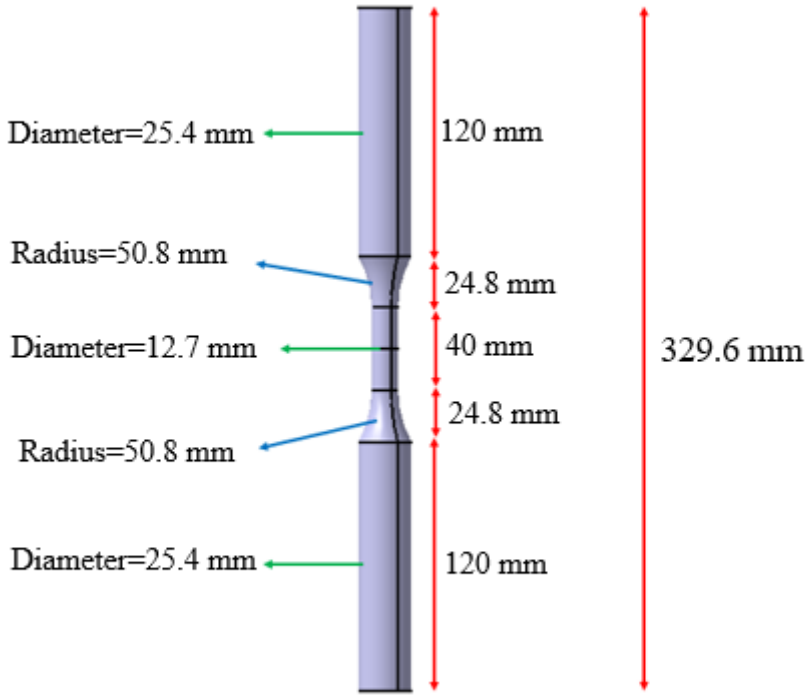

Figure 5.1: Dimensions of Manufactured Coupons

Figure 5.2: Test Setup

5.2 Uniaxial Tensile Test Results

After the first test was conducted, to eliminate the effects of cold working and obtain higher ductility, an annealing procedure was conducted for the rest of the samples. They were heated to 850°C, kept in the oven for 1 hour, and cooled in the oven [51]. As received and annealed force-displacement curves of the specimens are shown in Figure 5.3, and as it can easily seen the ductility of metal increased and its UTS decreased at the end of the annealing process.

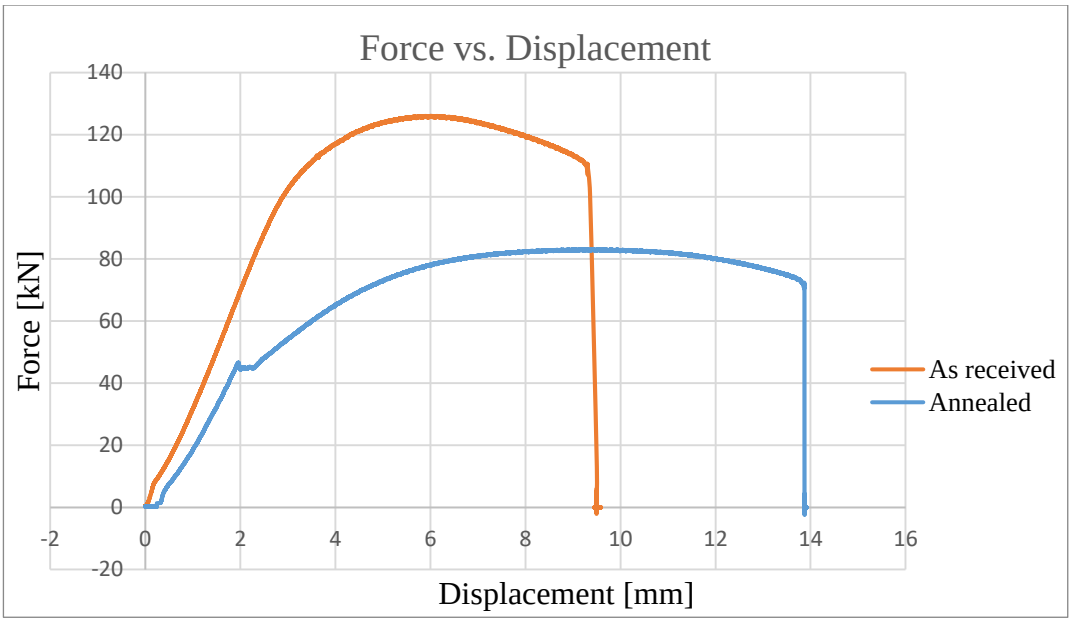

Figure 5.3: Force vs. Displacement Curve of As Received and Annealed Test

After the annealing process, 2 uniaxial tests were performed and the extensometer was removed after a short time from the onset of necking to protect the device against breakage. Hence, the stress-strain data could not be obtained until the complete fracture. The results of the two tests are shown in Figure 5.4 indicating that both tests give very close results. As a result, the mechanical properties of the AISI 4140 were tabulated in Table 5.1. Note that density and Poisson's ratio were obtained from the literature [52] and to express the behavior of material in the plastic region, nonlinear kinematic hardening constants (c and γ) were obtained after entering true stress and true plastic strain data, then using half cycle property of ABAQUS software and reading its input file.

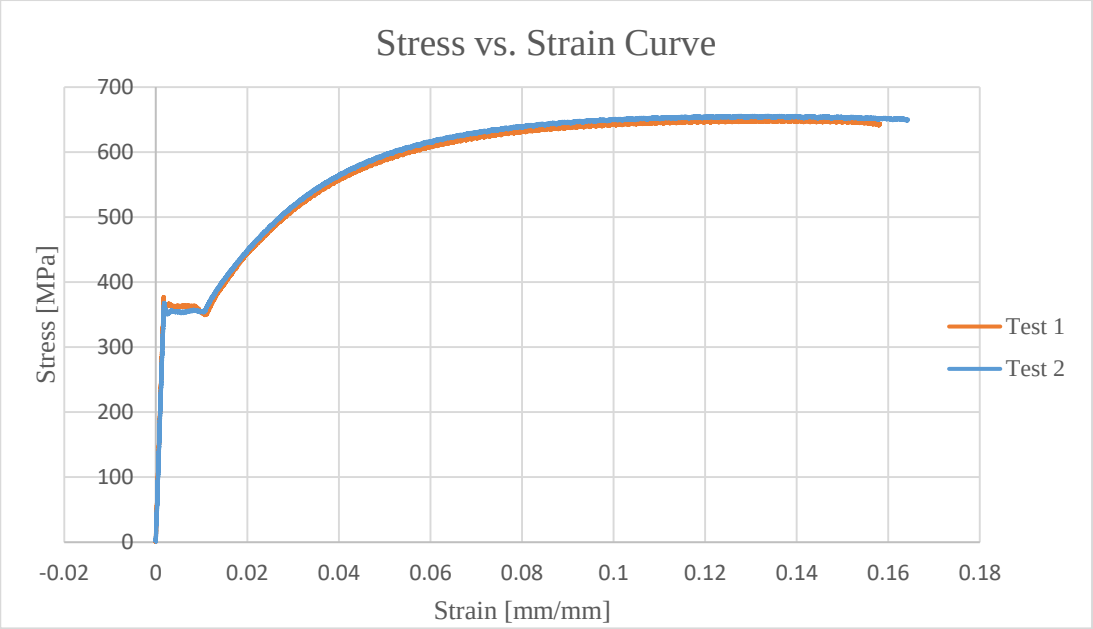

Figure 5.4: Engineering Stress vs. Strain Curve for Uniaxial Tensile Tests

Table 5.1: Mechanical Properties of AISI4140

$E\ [GPa]$	ϑ	$\sigma_Y\ [MPa]$	$\sigma_{UTS}\ [MPa]$	$c\ [MPa]$	γ	$\rho\ [kg/m^3]$
206	0.3	351	655	8246	19	7850

5.3 Experimental Studies on Fatigue Failure

In order to examine fatigue failure, four experiments having different stress amplitude and mean stress values were conducted by using test setup which is shown in Figure 5.2Figure 5.2: Test Setup. All tests were performed at 1 Hz frequency. Tests were conducted by loading and unloading and since there is no compression in the tests, the mean stress values are half of the stress amplitude values. The results of these tests are presented in Table 5.2. Moreover, the fracture surfaces of the specimens are shown in Figure 5.5-Figure 5.8.

Table 5.2: Fatigue Test Results

Test No	σ_a [MPa]	σ_M [MPa]	Number of Cycles	Type
1	514	257	34150	HCF
2	537	268.5	31936	HCF
3	551	275.5	14241	HCF
4	598	299	969	LCF

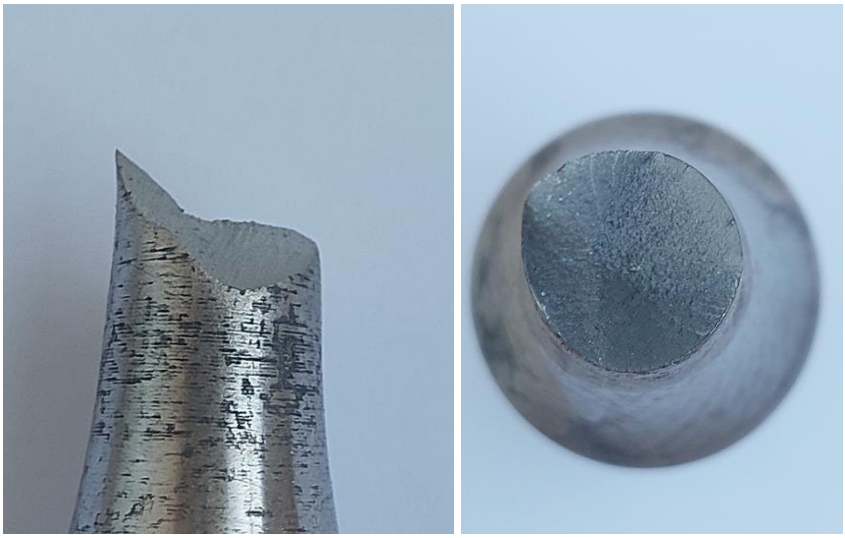

Figure 5.5: Side and Top Views of Fracture Surface at Fatigue Test 1

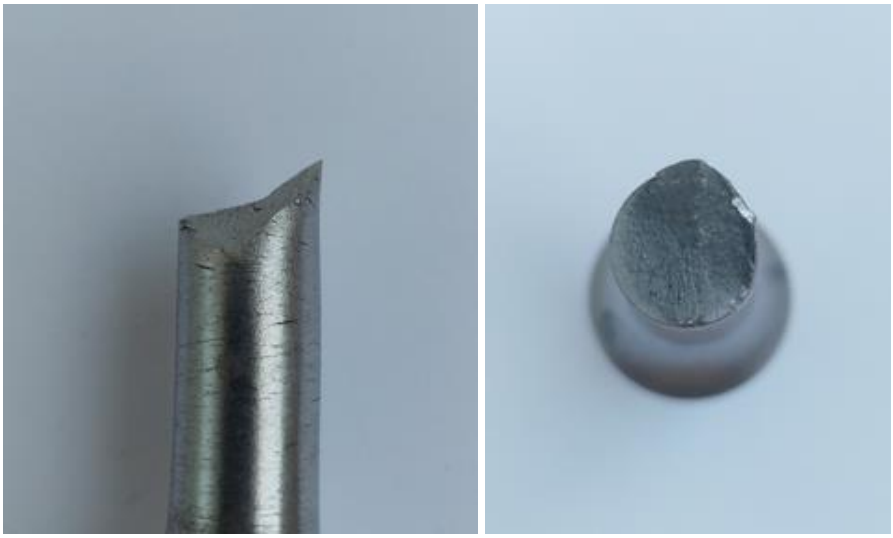

Figure 5.6: Side and Top Views of Fracture Surface at Fatigue Test 2

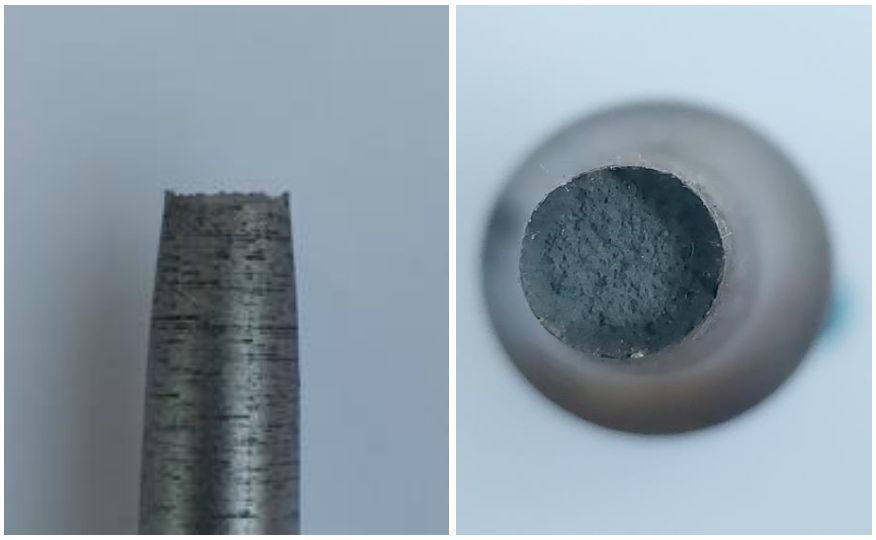

Figure 5.7: Side and Top Views of Fracture Surface at Fatigue Test 3

Figure 5.8: Side and Top Views of Fracture Surface at Fatigue Test 4

When the test results in Table 5.2 and the fracture view of the surfaces in Figure 5.5 to Figure 5.8 are examined, it can be concluded that as the number of cycles to failure increases, the fracture type becomes brittle. It can be easily seen from Figure 5.5 that the fracture is brittle with a small reduction at the crossectional area, on the other hand, for test 4, the fracture is ductile with cup and cone fracture type and the crossectional area reduction is higher as shown in Figure 5.8 . Therefore, LCF failure

types result in more ductile type fracture than HCF and this makes using a ductile fracture criteria to determine LCF failure more appropriate.

This thesis considers fatigue cases having both loading and reverse loading. However, the performed tests were conducted by loading and unloading due to the limitations of the test setup. Since these tests do not give any information for compressive behavior, they were not simulated to verify the fatigue failure criteria based on UDFC.

The results of these tests show that increasing stress amplitude and mean stress affect the ductility of failure and the number of cycles. Therefore, these parameters must be included in the determination of fatigue failure criteria based on UDFC.

CHAPTER 6

RESULTS AND DISCUSSION

6.1 Evaluation of Monotonic Failure Results

To obtain UDFC constants at the onset of necking, the simulation of the conducted tensile test was performed with the same loading type and rate (0.05 mm/s), and these constants were determined when the onset of necking was reached. After the onset of necking is observed, the equivalent plastic strain values increase dramatically [49]. Variation of the equivalent plastic strain with respect to time during the tensile test is shown in Figure 6.1, and its distribution at the onset of necking is shown in Figure 6.2. Moreover, this point was determined by the stress wave propagation method which was also verified by the force-displacement curve of the test, as shown in Figure 6.3. This figure shows that the numerical and experimental results of the force-displacement relation until the onset of necking are very close. Since all comparisons in this thesis were made at the onset of necking, the difference between the test and FEM after the onset of necking did not affect the results. It can be concluded that the onset of necking can be successfully determined by FEM as Figure 6.3 shows. Therefore, the UDFC constants were obtained through FEA and tabulated in Table 6.1 for further calculations.

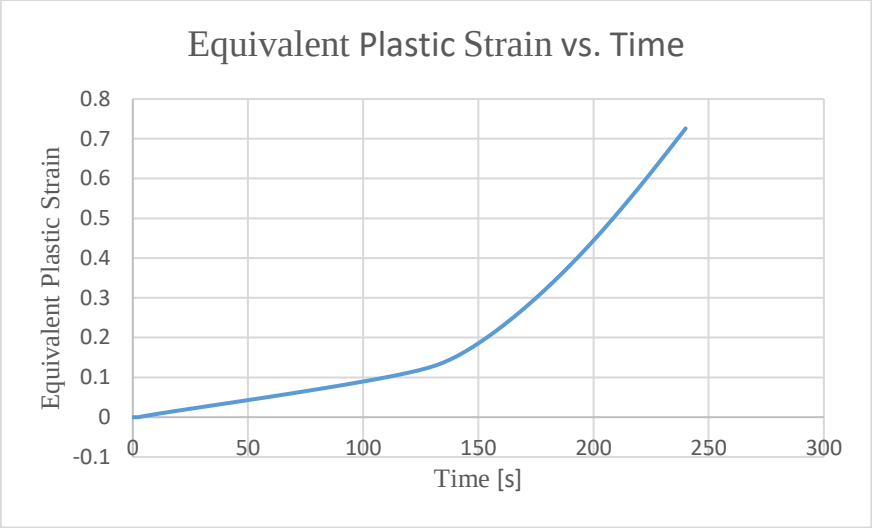

Figure 6.1: Equivalent Plastic Strain Variation in Tensile Test Simulation

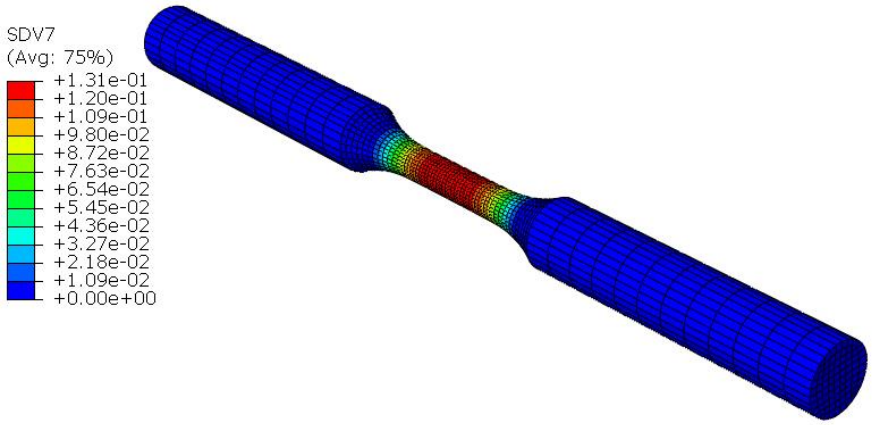

Figure 6.2: Equivalent Plastic Strain Distribution at the Onset of Necking

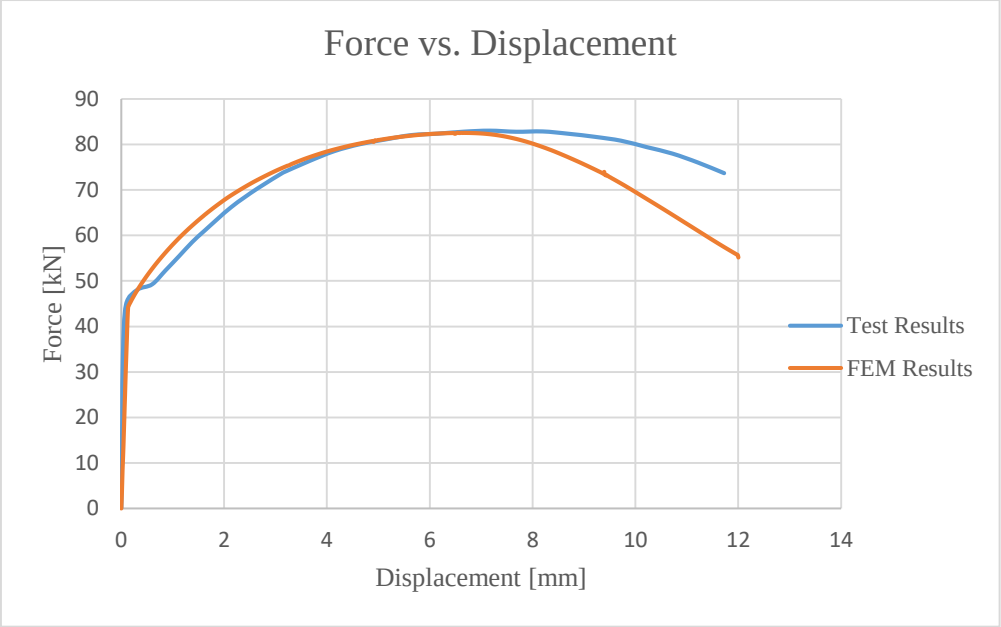

Figure 6.3: Comparison of Force-Displacement Curve for Test and FEM

Table 6.1: UDFC Constants Obtained From Necking Point

Freudenthal	Cockroft-Latham	Ayada	Oyane-Sato	Oh
81.7	81.8	0.0436	0.0872	0.131

6.2 Low-Cycle Fatigue Results

After tensile test simulation was performed and UDFC constants of the five criteria were extracted from the necking point of the simulation, the low-cycle fatigue simulations were performed by using sinusoidal forces having different amplitude, mean, and frequency values. In these simulations, UDFC constants and the number of cycles were recorded in the step before the equivalent plastic strain values were localized in a specific location (the onset of necking). The results of these simulations were used to obtain a relation between the new constants based on UDFC and the number of cycles at the onset of necking.

6.2.1 Effects of Parameters on the Results

In this section, the effects of frequency, stress amplitude and mean stress on UDFC-based constants were presented. The constants were determined at the onset of necking, that is, when equivalent plastic strain values are localized. While the effect of one parameter was investigated, others were kept constant. Since some UDFC are stress-based and others are nondimensional, to compare them clearly, all of them were nondimensionalized by dividing to their tensile test values as shown in Table 6.1. In addition, these nondimensionalized values were called as "UDFC-based factor" for further calculations and discussion.

Since low-cycle fatigue tests are suggested to be carried out at frequencies up to 5 Hz [53], by keeping the mean stress value and stress amplitude constant, the effect of increasing frequency was examined up to this value. For this purpose, under 357 MPa stress amplitude and 70 MPa mean stress, the nondimensionalized UDFC-based factors for simulations having frequencies between 0.5 Hz and 5 Hz were calculated at the necking point and presented in Figure 6.4. From this figure, it can be said that for Freudenthal, Oh, and Oyane-Sato criteria close relation were obtained. Moreover, it is seen that there is a sudden jump at 3.5 Hz. For Ayada this sudden change is 36%, for Cockroft-Latham, it is 27%, and since the rest of the three criteria have similar relation, for them it is 25%.

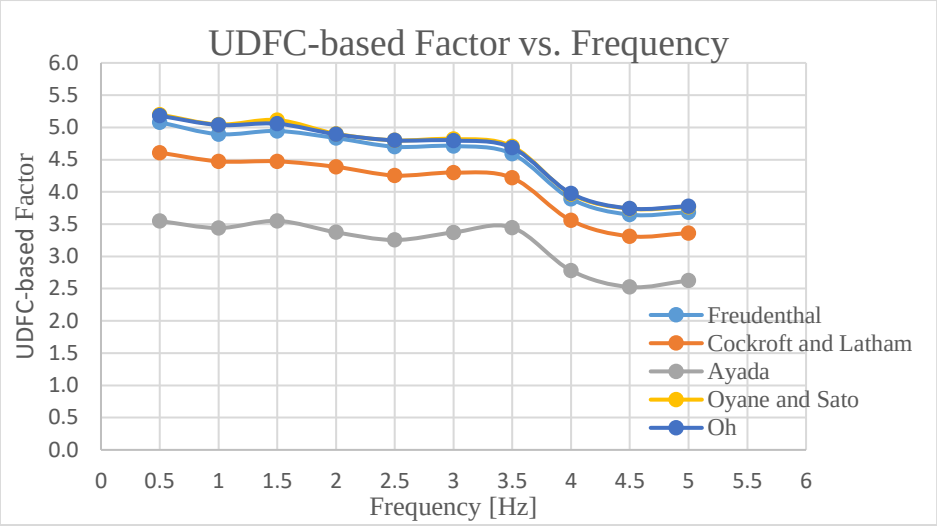

Figure 6.4: Effect of Frequency on UDFC-based factor

As it is seen in Figure 6.5, as mean stress increases at a constant frequency of 1 Hz and a constant stress amplitude of 357 MPa, all UDFC-based factors decrease. In addition, the reduction of this factor is smallest in Ayada and highest in Freudenthal, Oyane-Sato, and Oh which are almost similar to each other.

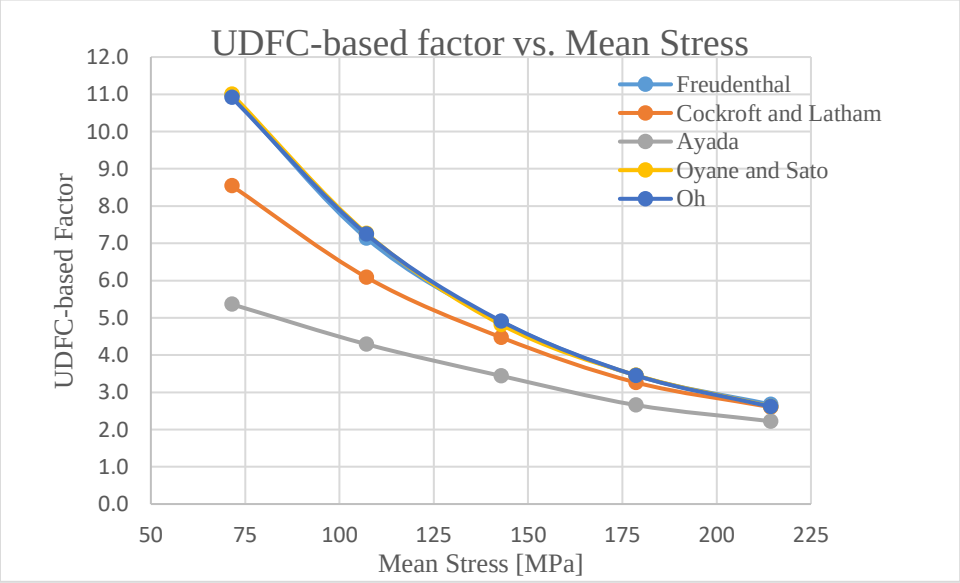

Figure 6.5: Effect of Mean Stress on UDFC-based factor

Figure 6.6 shows that as stress amplitude increases at the constant frequency of 1 Hz and the mean stress of 70 MPa, all UDFC-based factors decrease. Additionally, the reduction of this factor is smallest in Ayada and highest in Freudenthal. Whereas, Oyane-Sato and Oh give a relation slightly lower than Freudenthal.

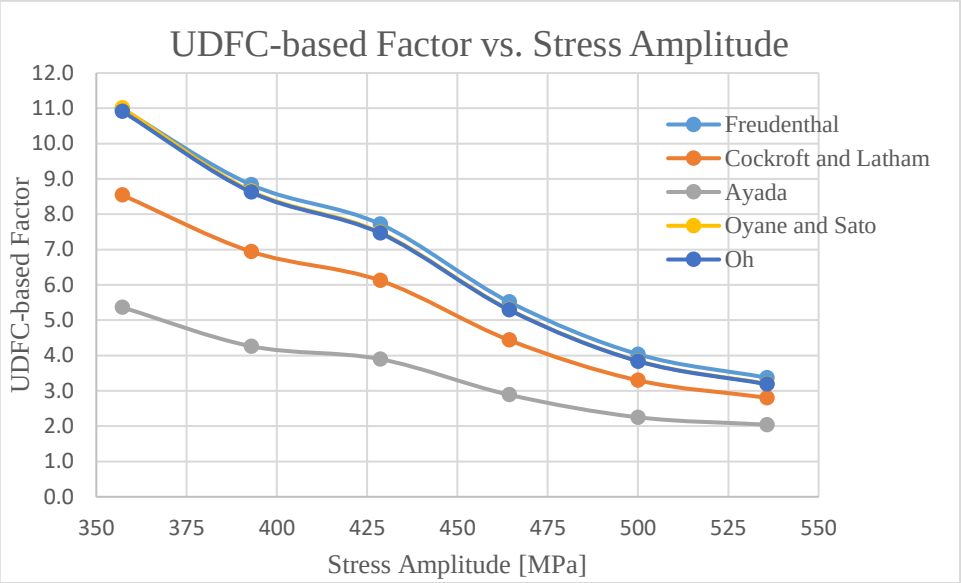

Figure 6.6: Effect of Stress Amplitude on UDFC-based factor

As a result of these comparisons, it can be concluded that mean stress and stress amplitude have a major effect on UDFC-based factors. Therefore, they must be used as an input for UDFC-based factor calculation Further, frequency effects must be added to these functions as a reduction factor if the frequency value is greater than 3.5 Hz.

6.2.2 Energy and Life Functions

In this section, a method is developed to calculate the UDFC-based factors for 5 criteria by using two functions which are called FFC function $\varphi(\sigma_a, \sigma_m)$ and life function $N(\varphi(\sigma_a, \sigma_m))$. The main goal of the FFC function is to relate the intended UDFC-based factor by stress amplitude and mean stress at a constant frequency of 1 Hz. The life function is aimed to find the life of the structure by using the UDFC-based factor. These two functions were calculated according to their inputs with the help of the curve fitting toolbox of the MATLAB software and were chosen as polynomial functions due to their simplicity and accuracy as a function type. For FFC functions except Ayada, second-order polynomials were used because it was seen that although an increase in the degree of polynomial increases the R^2, constants of higher-order terms have no significant effect. For Ayada, a first-order function was used. A third-order polynomial was preferred to determine the life function since a second-order polynomial cannot cover the relation in lower values of life when it is a parabola. As a result, the functions are obtained as given below and their constants are tabulated in Table 6.2 and Table 6.3.

The general form of FFC function (φ)is:

$$\varphi(\sigma_a, \sigma_m) = d_1 + d_2\sigma_a + d_3\sigma_m + d_4\sigma_a\sigma_m + d_5\sigma_m^2 \quad (6.1)$$

The general form of life function function (N) is:

$$N[\varphi(\sigma_a, \sigma_m)] = n_1\varphi(\sigma_a, \sigma_m)^3 + n_2\varphi(\sigma_a, \sigma_m)^2 + n_3\varphi(\sigma_a, \sigma_m) + n_4 \quad (6.2)$$

Using Equation 6.1, the fatigue failure criterion (FFC) is obtained as follows:

$$\Phi(\sigma_a, \sigma_m) = \varphi(\sigma_a, \sigma_m) - E_t = 0 \quad (6.3)$$

where E_t is energy-based damage accumulation value for the related UDFC.

Table 6.2: FFC Function Constants

Criteria	d_1	d_2	d_3	d_4	d_5
Freudenthal	47.500	-0.0700	-0.3274	0.0003	0.0006
Cockroft-Latham	31.530	-0.0471	-0.1770	0.0002	0.0003
Ayada	12.150	-0.0171	-0.0189	0.0000	0.0000
Oyane-Sato	47.140	-0.0721	-0.3108	0.0004	0.0005
Oh	46.900	-0.0714	-0.3097	0.0003	0.0005

Table 6.3:Life Function Constants

Criteria	n_1	n_2	n_3	n_4
Freudenthal	0.0385	-0.3571	4.594	-6.103
Cockroft-Latham	0.0799	-0.1372	2.783	-3.153
Ayada	0.434	0.9282	-3.363	3.224
Oyane-Sato	0.0339	-0.2042	3.668	-4.843
Oh	0.0322	-0.1673	3.483	-4.619

After determining these functions, their R^2 values were calculated by using the failure points of the performed simulations, and they were tabulated in Table 6.4. Among these criteria, it is seen that Freudenthal has the highest R^2 for FFC function, and the lowest R^2 for life function. On the other hand, Ayada has the lowest R^2 value for FFC function, and the highest R^2 for life function. Oyane-Sato and Oh give again similar accuracy as their relationships are very close. If R^2 values of two functions were examined, it can be concluded that the best criterion is the C-L criteria.

Table 6.4: R^2 Values of Functions

Function	Freudenthal	C-L	Ayada	O-S	Oh
FFC function	0.9837	0.9784	0.9399	0.9843	0.9844
Life Function	0.8487	0.8955	0.9190	0.8755	0.8746

After obtaining each function with their constants, they are plotted using their failure points. The fatigue life prediction of these criteria is given as follows:

- *Freudenthal*

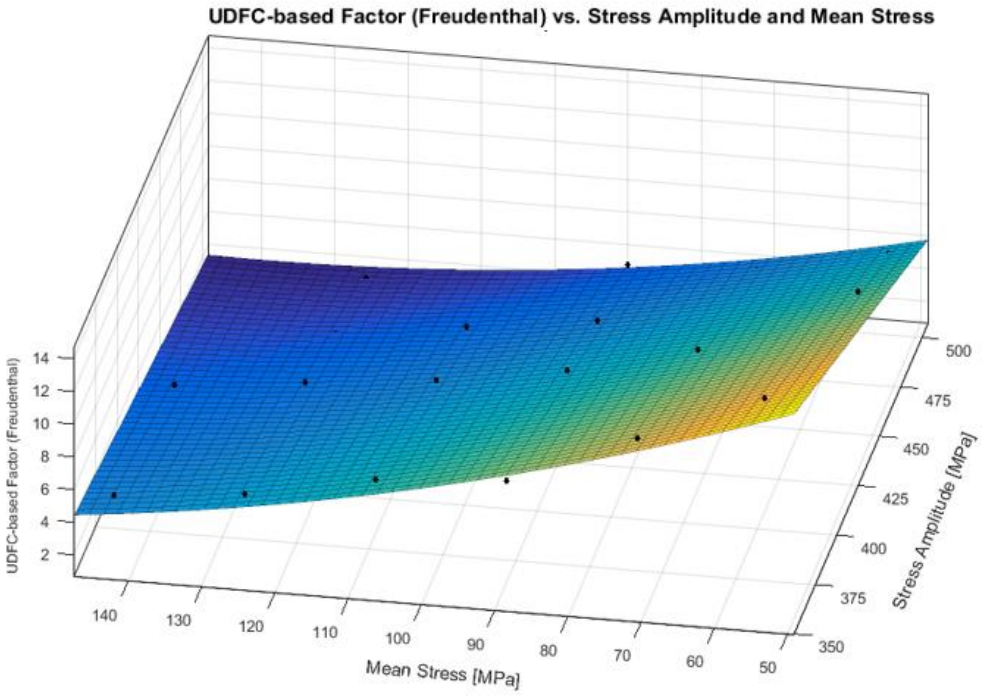

Figure 6.7: Surface of Freudenthal FFC function

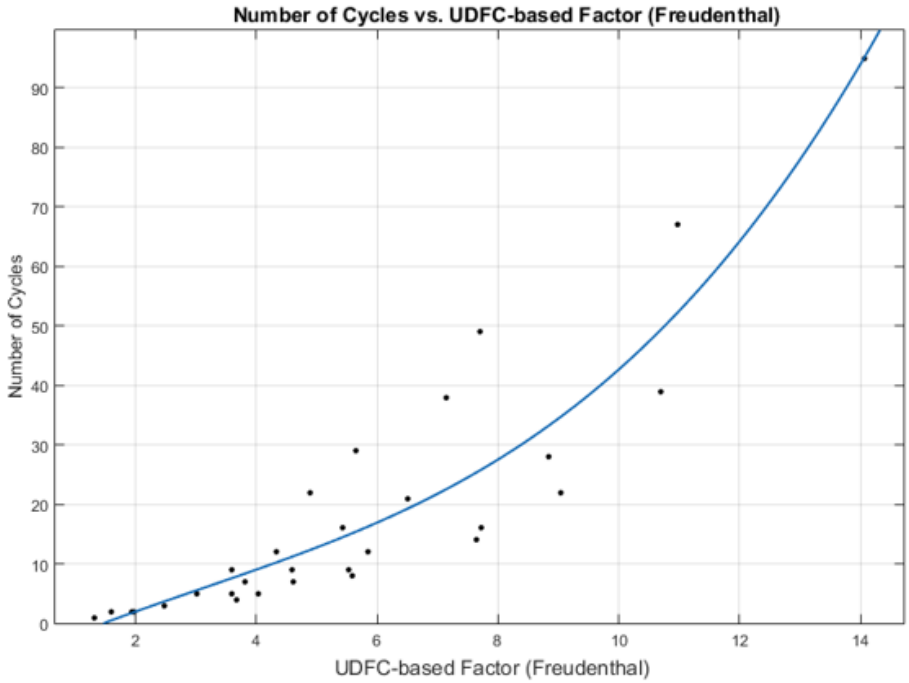

Figure 6.8: Curve of Freudenthal Life Function

- *Cockroft-Latham*

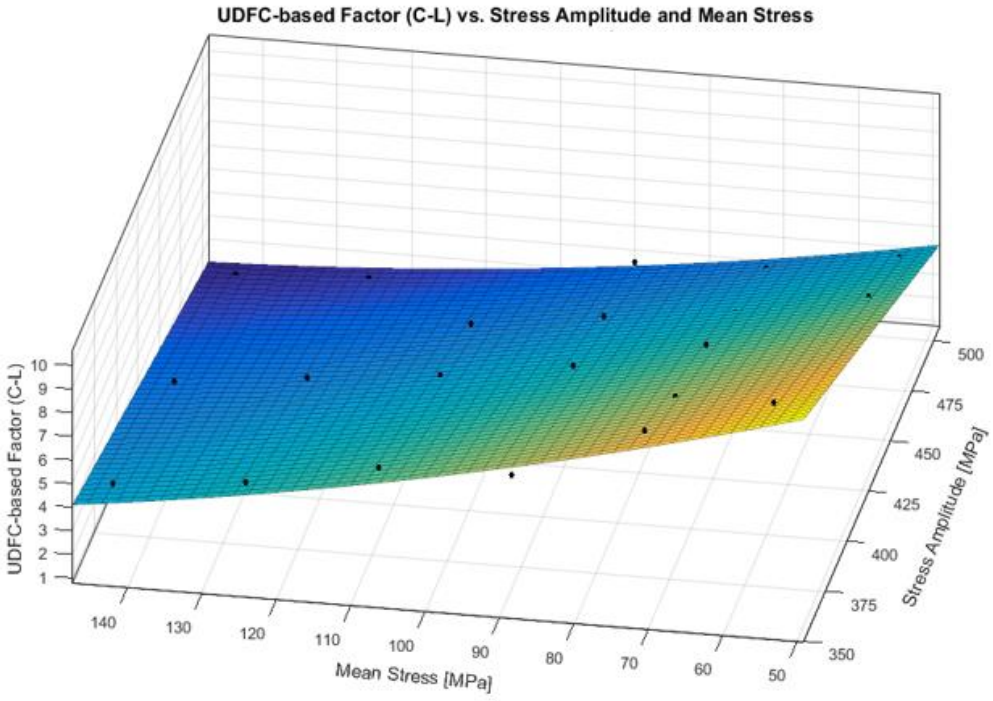

Figure 6.9: Surface of Cockroft-Latham FFC Funciton

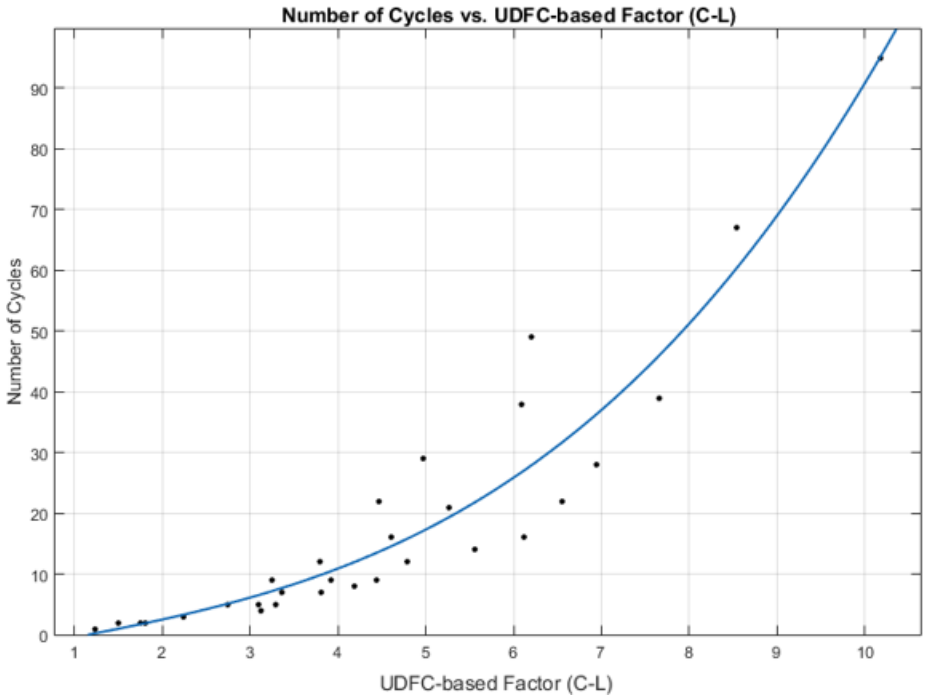

Figure 6.10: Curve of Cockroft-Latham Life Function

- *Ayada*

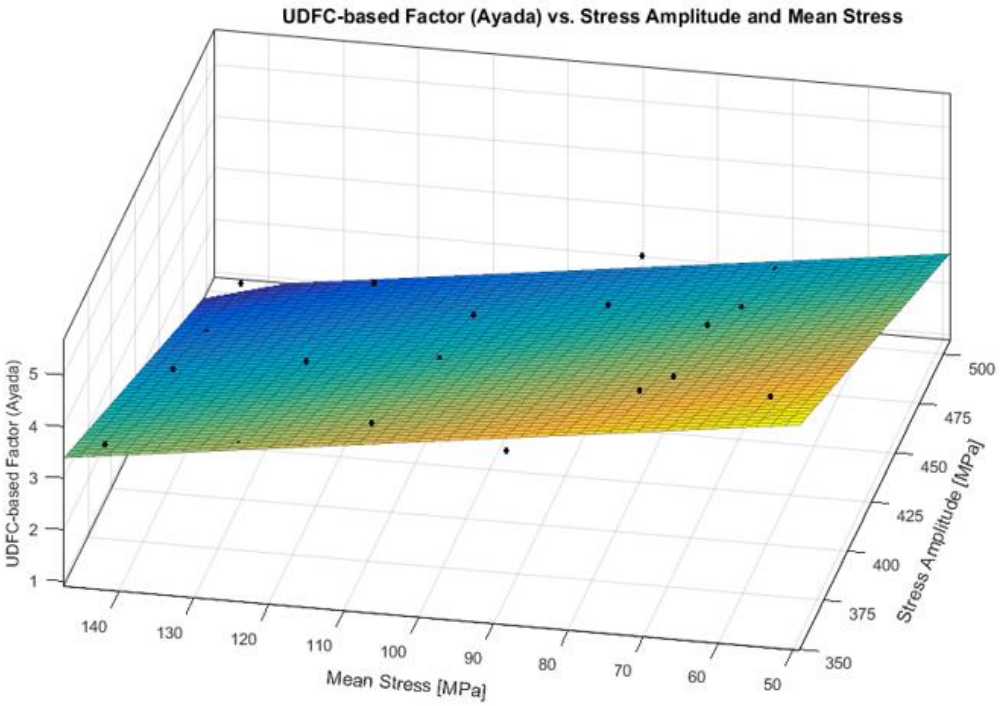

Figure 6.11: Surface of Ayada FFC Funciton

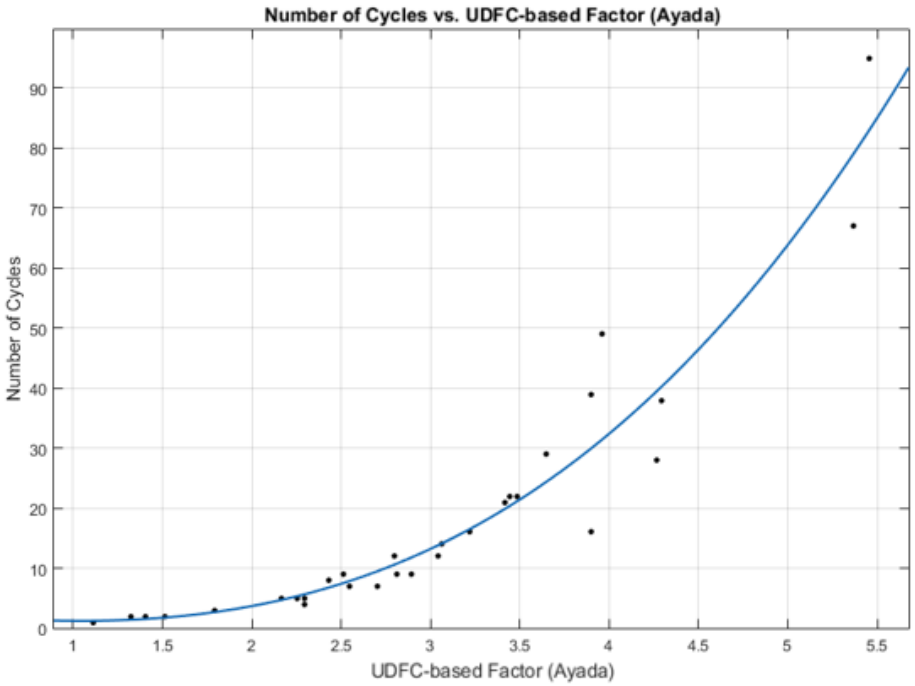

Figure 6.12: Curve of Ayada Life Function

- *Oyane-Sato*

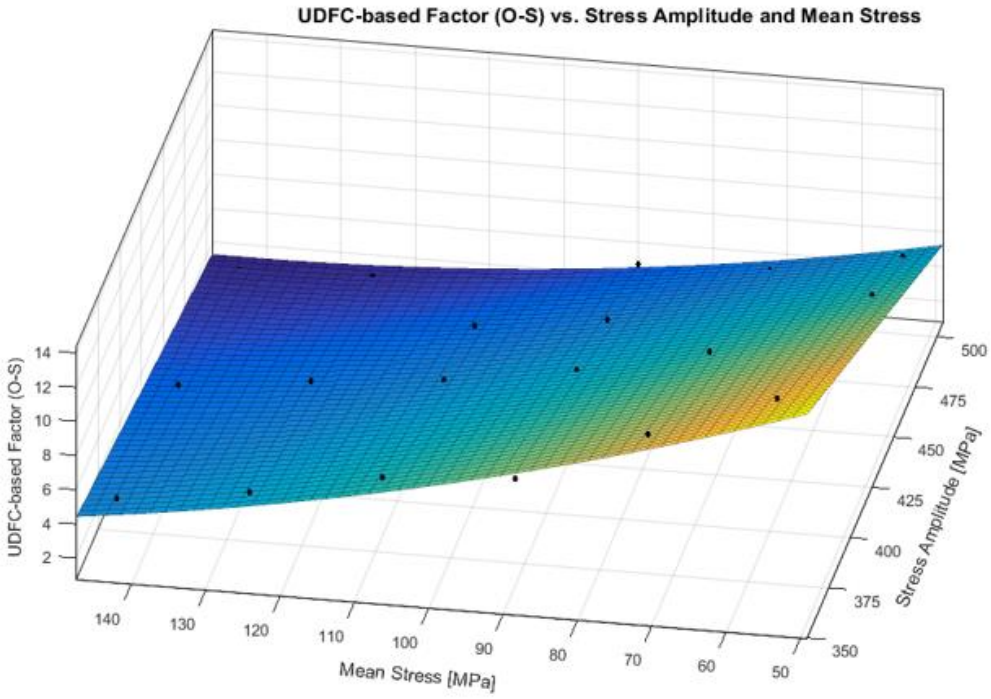

Figure 6.13: Surface of Oyane-Sato FFC Funciton

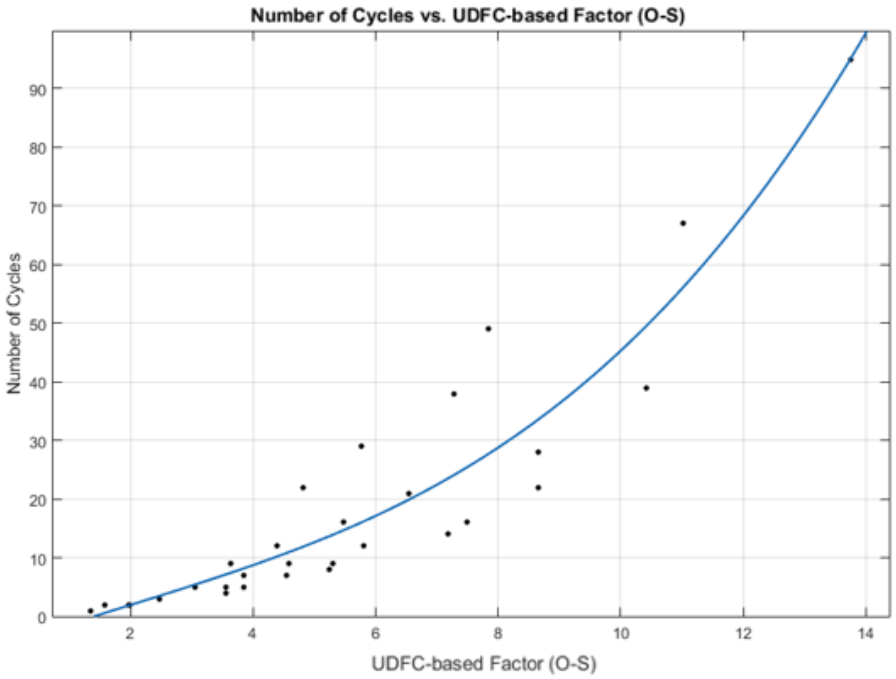

Figure 6.14: Curve of Oyane-Sato Life Function

- *Oh*

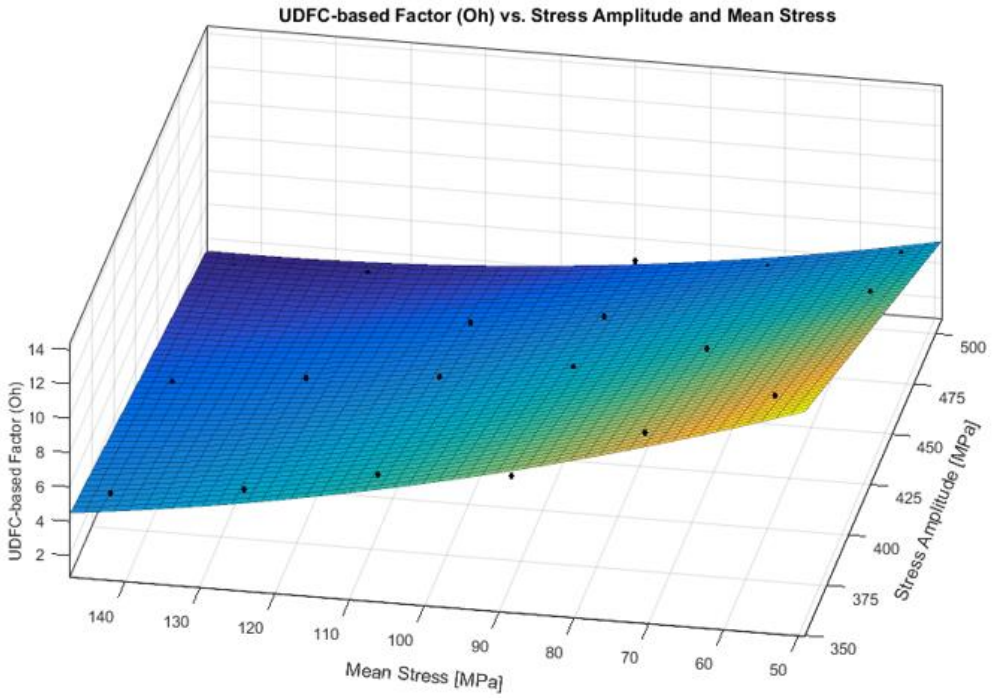

Figure 6.15: Surface of Oh FFC function

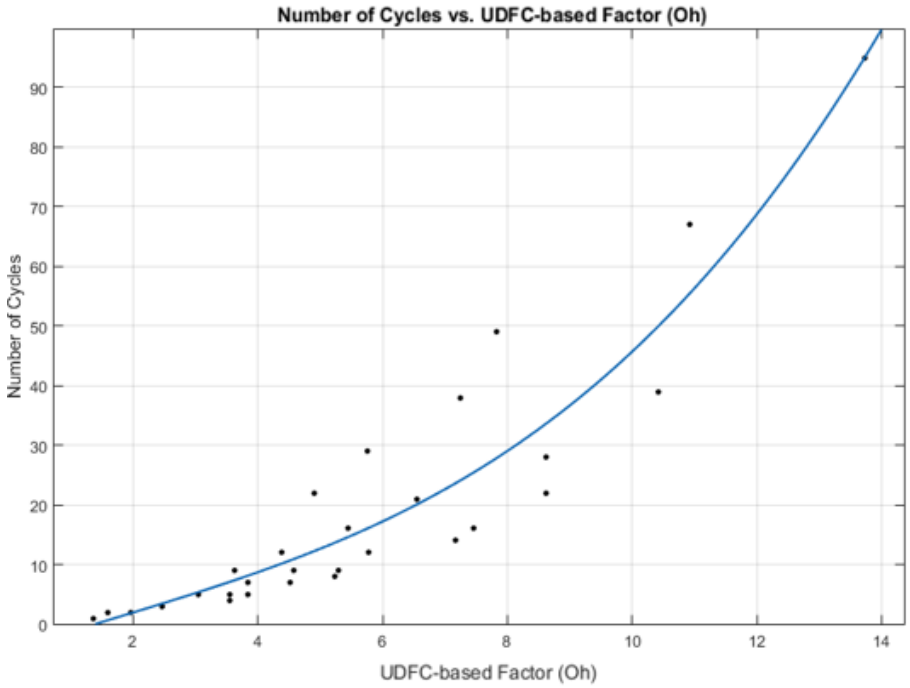

Figure 6.16: Curve of Oh Life Function

From Figure 6.7 to Figure 6.16, it can be seen that by FFC functions surfaces are defined, whereas by life functions curves are obtained. Since these surfaces are obtained from the failure points, for the damage accumulation values below these surfaces, structures do not exhibit fatigue failure. All these surfaces and curves were found at the frequency of 1 Hz. Therefore, as mentioned in the previous section, when the frequency is higher than 3.5 Hz a reduction was observed in damage accumulation of all criteria. Therefore, if the excitation frequency of the structure is higher than 3.5 Hz, these curves and surfaces must be shifted below by the percentage discussed in section 6.2.1. As a result of this work, a designer can find the damage accumulation value of a cyclic loading at desired mean stress, stress amplitude and frequency, hence defining whether there is fatigue failure and also the life of a structure with respect to damage accumulation value of no fatigue failure. For this purpose, uniaxial tensile test and fatigue simulations are used.

6.2.3 The Performance of the Selected Functions

To verify the performance of these functions, 5 cases shown in Table 6.5 with randomly selected stress amplitude and mean stress values were analyzed in ABAQUS, and their UDFC-based factor and life results were compared in Table 6.6 and Table 6.7.

Table 6.5: Stress Amplitude and Mean Stress Values of Test Cases

Case Name	σ_a $[MPa]$	σ_m $[MPa]$
Case 1	396	75
Case 2	457	109
Case 3	492	120
Case 4	444	81
Case 5	371	64

Table 6.6: UDFC Constants of Test Cases by FEM and FFC function

Name	Results	Freudenthal	C-L	Ayada	O-S	Oh
Case 1	FEM	1.96	1.76	1.45	1.98	1.97
	Function	1.93	1.82	1.48	1.96	1.93
	Error [%]	1.88	3.10	2.17	1.02	2.00
Case 2	FEM	3.32	2.88	2.13	3.30	3.30
	Function	3.43	3.05	2.29	3.46	3.44
	Error [%]	3.28	5.97	7.27	4.86	4.22
Case 3	FEM	5.34	4.35	2.91	5.21	5.20
	Function	5.83	4.68	3.04	5.73	5.71
	Error [%]	9.16	7.47	4.45	10.14	9.79
Case 4	FEM	8.22	6.47	3.99	8.09	8.07
	Function	8.49	6.59	3.97	8.41	8.37
	Error [%]	3.29	1.76	0.45	3.95	3.76
Case 5	FEM	10.97	8.26	4.83	10.89	10.82
	Function	10.96	8.21	4.61	10.81	10.77
	Error [%]	0.04	0.66	4.61	0.69	0.43

As it is seen in Table 6.6, for the different cases, the difference between the results of the FFC function changes. This difference can be attributed to the curve fitting performance. However, by looking at the results, it is seen that the highest error is 10.14% for the Oyane-Sato FFC function. From previous results, it is known that, when the UDFC-based factor decreases, life decreases also. Therefore, a reduction in the UDFC-based factor results in a conservative solution. As a result, the maximum error in each criterion can be used as a safety factor for that function. For example, if the Oyane-Sato function is used, a 10.14% reduction factor can be used.

Table 6.7:Number of Cycles by Life Functions and FEM

Name	Freudenthal	C-L	Ayada	O-S	Oh	FEM
Case 1	2	2	2	2	2	2
Case 2	7	6	6	7	7	5
Case 3	16	15	14	16	16	10
Case 4	31	32	32	32	32	25
Case 5	52	55	50	54	54	50

In Table 6.7, the number of cycles obtained by 5 life functions based on different UDFC criteria and FEM are compared. Note that although the life functions give the results with decimals, Table 6.7 shows them by rounding up to the closest integer. As a result of this comparison, it can be said that among these 5 criteria, Ayada has the highest accuracy for predicting life value. However, taking the highest error in Ayada which is taken from case 3 in Table 6.7, a 40% safety factor must be used for life calculation. If other criteria were used this safety factor must be higher.

As a result of this work, providing that tensile test data of a material is known, the amount of damage accumulation in the material can be calculated for a specific stress amplitude and mean stress at a specific frequency. Moreover, by using this damage accumulation value, the number of cycles to failure can be found also.

CHAPTER 7

CONCLUSION AND FUTURE WORK

7.1 Conclusion

In this thesis, five uncoupled ductile fracture criteria (UDFC) namely Freudenthal, Cockroft-Latham, Ayada, Oyane-Sato, and Oh are used to determine low-cycle fatigue life calculation of AISI 4140 steel. For this purpose, a tensile test for obtaining mechanical properties, and a commercial FEA software for performing fatigue simulations and calculating damage accumulation values are used. In all simulations, failure is calculated at the onset of necking, and this point is found by the stress wave propagation method provided by the used software. After performing many analyses having different stress amplitude and mean stress values, in this work, the following are concluded:

1- It is observed that failure values for all five criteria defined by UDFC-based factors show a close relationship up to 5 Hz. However, at 3.5 Hz, these values decrease to a lower value maintaining the same trend. This work proposes a method to determine the low-cycle fatigue for frequencies less than 3.5 Hz. For frequencies higher than 3.5 Hz, it is recommended to determine a reduction factor to use with the proposed method.
2- It is observed that when stress amplitude increases at constant mean stress or mean stress increases at a constant stress amplitude, fatigue life decreases.
3- It is found that different mean stress and strain amplitude values, that is, different damage accumulation values tend to cluster around a curve. Hence, a single fatigue life versus FFC function curve can be obtained with an acceptable accuracy.
4- As the number of cycles to fatigue failure increases, damage accumulation values also increase. However, for a single cycle to failure the damage

accumulation value is almost the same as that obtained in a simple tension test.

5- For better comparison, since damage accumulation values have different units, it is found appropriate to nondimensionalize the damage values of cyclic loading simulations by dividing them to the values from the simple tension test which are referred to as UDFC-based factors.

6- By considering the results of many simulations based on five UDFCs three equations are obtained to determine the fatigue failure; the FFC function which is a function of mean stress and stress amplitude and can be represented by a surface, the life function which depends on the FFC function and plotted as a curve, and the fatigue failure criteria, FFC.

7- It is observed that the accuracy of all FFC functions is close to the values found from numerical simulations.

8- The investigation of the effectiveness of life function showed that, among those based on different UDFC, the Ayada criterion has the highest accuracy.

9- As a result, by the FFC function, the damage accumulation of a material is calculated by using the applied mean stress and stress amplitude at a defined frequency. Additionally, the life function, by using the damage accumulation of material, gives the life of a material at the current cyclic loading. Finally, FFC is utilized to define the fatigue for a specific material and loading.

7.2 Future Work

Although the proposed models of this thesis represent low-cycle fatigue life calculation, they are not evaluated for high-cycle fatigue. As a future work, high-cycle fatigue life calculation can be studied by using uncoupled ductile fracture criteria. In this thesis, only constant amplitude loading cases were considered. In future work, cases including variable loading history can be examined. In this thesis, only uniaxial fatigue loading was performed, in future work, different fatigue loadings such as torsional, and biaxial loading, etc. can be examined. The presented functions and their constants belong to AISI 4140 steel, as a future work, these functions can be extended for different isotropic materials by adding some material properties.

REFERENCES

[1] R. Li, Z. Zheng, M. Zhan, H. Zhang, X. Cui, and Y. Lei, “Fracture prediction for metal sheet deformation under different stress states with uncoupled ductile fracture criteria,” Journal of Manufacturing Processes, vol. 73, pp. 531–543, Jan. 2022.

[2] R. G. Budynas and K. J. Nisbett, Shigley's Mechanical Engineering Design. 10th ed. New York, NY: McGraw-Hill Education, 2022.

[3] M. Albert, "On the theory of elasticity," Journal of Mathematics and Physics, vol. 1, pp. 1-25, 1837.

[4] G. Morin, "Study on the axles of railway wagons," Annales des ponts et chaussées, vol. 5, pp. 155-186, 1853.

[5] B. Braitwaite, "On the construction and strength of axles for railway carriages and wagons," Minutes of the Proceedings of the Institution of Civil Engineers, vol. 13, pp. 90-100, 1854.

[6] L. Wöhler, "Experiments on the strength properties and behavior of different materials under varying loads," Journal of the Society of German Engineers, vol. 4, pp. 1-88, 1860.

[7] F. Spangenberg, "Stress-strain relationships in fatigue," Journal of Applied Physics, vol. 7, no. 7, pp. 335-339, 1936.

[8] A. W. Soderberg, "Mechanical and physical properties of materials for machine elements," Transactions of the ASME, vol. 52, pp. 15-22, 1930.

[9] J. Goodman, "The fatigue of metals under repeated stresses," Transactions of the ASME, vol. 20, pp. 354-358, 1899.

[10] M. Gerber, "Ermüdungsfestigkeit," Zeitschrift des Vereines Deutscher Ingenieure, vol. 55, pp. 129-132, 1911.

[11] R. Basquin, "The fatigue of metals under repeated stress," Bulletin of the Society of French Engineers, vol. 10, pp. 633-662, 1910.

[12] W. Manson and L. F. Coffin, "A study of the fatigue characteristics of some metals," Transactions of the ASME, vol. 72, pp. 247-258, 1950.

[13] R. A. Smith, P. Watson, and T. H. Topper, "A stress-strain function for the fatigue of metals," Journal of Materials, vol. 4, no. 3, pp. 265-278, 1966.

[14] J. D. Morrow, "Mean stress effects on fatigue properties of metals," Journal of Applied Mechanics, vol. 45, no. 4, pp. 651-655, 1978.

[15] J. Jasper, "On the deformation properties of metallic crystals," Physikalische Zeitschrift, vol. 21, pp. 649-655, 1920.

[16] M. Enomoto, "On the transformation of elastic energy into plastic energy," Transactions of the Japan Society of Mechanical Engineers, vol. 21, no. 126, pp. 855-861, 1955.

[17] F. A. Stowell, "Transformation of elastic energy into plastic energy," Journal of the Mechanics and Physics of Solids, vol. 14, no. 2, pp. 99-110, 1966.

[18] C. E. Feltner and J. D. Morrow, "Microplastic strain hysteresis energy as a criterion for fatigue fracture," J. Basic Eng. Trans., ASME, vol. 83, pp. 15–22, 1961.

[19] A. Tresca, "On the flow of solids under stress," Comptes Rendus de l'Académie des Sciences, vol. 33, pp. 349-354, 1851.

[20] R. von Mises, "Mechanics of solid materials in the plastic state," Göttinger Nachrichten, Math.-Phys. Klasse, vol. 1, pp. 582-592, 1913.

[21] A. P. Boresi and R. J. Schmidt, Advanced Mechanics of Materials, 6th ed. Hoboken, NJ: Wiley, 2020.

[22] J. T. Ducker and W. Prager, "Elastic-plastic stress-strain relations," Journal of Applied Mechanics, vol. 19, no. 1, pp. 35-40, 1952.

[23] L. Ludwig, "On the conversion of elastic vibrations into plastic deformations," Annalen der Physik, vol. 333, no. 3, pp. 491-517, 1909.

[24] L. Prandtl and A. Reuss, "Remark on plasticity and strength," Journal of Applied Mathematics and Mechanics (Zeitschrift für Angewandte Mathematik und Mechanik), vol. 8, no. 3, pp. 85-87, 1928.

[25] W. Ramberg and W. R. Osgood, "Description of stress-strain curves by three parameters," Technical Note 902, National Advisory Committee for Aeronautics, 1943.

[26] C. G. Voce, "The relationship between stress and strain for homogeneous deformation," Journal of the Institute of Metals, vol. 74, no. 2, pp. 537-562, 1948.

[27] G. R. Johnson and W. H. Cook, "A constitutive model and data for metals subjected to large strains, high strain rates and high temperatures," Proceedings of the 7th International Symposium on Ballistics, The Hague, Netherlands, 1983, pp. 541-547.

[28] W. Bausinger, "On the alteration of elastic and plastic properties due to pre-straining and its technical significance," Archiv für Eisenhüttenwesen, vol. 27, no. 4, pp. 375-384, 1956.

[29] Prager W., A new method of analyzing stress and strains work-hardening plastic solids. Journal of Applied Mechanics, 23, 493-496, 1956.

[30] H. Ziegler, "A modification of Prager's hardening rule," Quarterly of Applied Mathematics, vol. 17, no. 1, pp. 55-59, 1959.

[31] R. W. Armstrong and C. O. Frederick, "A mathematical representation of the multiaxial Bauschinger effect," in CEGB Report RD/B/N 731, Central Electricity Generating Board, Berkeley Nuclear Laboratories, Gloucestershire, U.K., 1966.

[32] B. Chaboche, "Time-independent constitutive theories for cyclic plasticity," International Journal of Plasticity, vol. 5, no. 3, pp. 247-302, 1979.

[33] B. Chaboche and J. Lemaître, "Mechanics of solid materials at high temperatures," International Journal of Solids and Structures, vol. 21, no. 6, pp. 541-553, 1985.

[34] K. Ohno and H. Wang, "Kinematic hardening rules with critical state of dynamic recovery, part I: formulation and basic features for ratchetting behavior," International Journal of Plasticity, vol. 9, no. 3, pp. 375-390, 1993.

[35] J. Lemaître and A. Menzel, "A new approach for modeling kinematic hardening in cyclic plasticity," International Journal of Plasticity, vol. 17, no. 6, pp. 723-748, 2001.

[36] L. M. Kachanov, "Time of the rupture process under creep conditions," Izvestiya Akademii Nauk SSSR, Otdelenie Tekhnicheskikh Nauk, vol. 8, pp. 26-31, 1958.

[37] A.L. Gurson, "Continuum theory of ductile rupture by void nucleation and growth, I. Yield criteria and flow rules for porous ductile media," J. Eng. Mater. Technol., vol. 99, no. 1, pp. 2-15, 1977.

[38] F.A. Freudenthal, The Inelastic Behavior of Engineering Materials and Structures. New York: Wiley, 1950.

[39] M.G. Cockroft and D.J. Latham, "Ductility and workability of metals," J. Inst. Metall, vol. 96, pp. 33-39, 1968.

[40] S.I. Oh, C.C. Chen, and S. Kobayashi, "Ductile fracture in axisymmetric extrusion and drawing," J. Eng. Ind. Trans. ASME, vol. 101, pp. 36-44, 1979.

[41] M. Ayada, T. Higashino, K. Mori, "Central bursting in extrusion of inhomogeneous materials," In Proceedings of the First ICTP. Adv. Tech. of Pals. Tokyo, Japan, 1, 553–558, 1984.

[42] Oyane, T. Sato, K. Okimoto and S. Shima, 1980, Criteria for ductile fracture and their applications, J. Mech. Work. Technol, Vol. 4, pp. 65-81.

[43] R. Hill, The Mathematical Theory of Plasticity. Oxford: Clarendon Press, 1950.

[44] Continuum Mechanics, "Von Mises Stress," Continuum Mechanics. [Online]. Available: https://www.continuummechanics.org/vonmisesstress.html.

[45] F. P. Dunne and N. Petrinic, Introduction to Computational Plasticity. Oxford: Oxford University Press, 2005.

[46] Dassault Systèmes Simulia Corp., "fe-safe Fatigue Theory Reference Manual," 2019.

[47] R. W. Hertzberg, Deformation and Fracture Mechanics of Engineering Materials. Wiley, 1983.

[48] Altair, Introduction to Explicit Analysis with Altair Radioss. Altair, 2017.

[49] S. A. Dizaji, “Evaluation of Post Necking Behavior of Metals Using Stress Wave Propagation Technique,” Trans Indian Inst Met, vol. 76, no. 11, pp. 3087–3094, Nov. 2023, doi: 10.1007/s12666-023-03044-7.

[50] M. Mashayekhi, "Writing User Subroutines with Abaqus," Source of the Presentation. [Online]. Available: https://mashayekhi.iut.ac.ir/sites/mashayekhi.iut.ac.ir/files//u32/presentation13.pdf.

[51] A. M. A. Wahab, E.-G. Mokhtar, and A. Mazen, “Effect of Heat Treatment on the Fracture Toughness of AISI 4140 Steel,” vol. 33, 2014.

[52] ASTM Steel, "AISI Alloy 4140 Steel Bar," ASTM Steel. [Online]. Available: https://www.astmsteel.com/product/aisi-alloy-4140-steel-bar/.

[53] ASTM International, "Standard Test Method for Strain-Controlled Fatigue Testing," ASTM E606-19, ASTM International, West Conshohocken, PA, 2019.